Submarine salt dissolution in the Santos Basin, offshore Brazil

C. R. Rodriguez[1§], C. A-L. Jackson[1], R. E. Bell[1], A. Rotevatn[2], M. Francis[3]

[1]*Basins Research Group (BRG), Department of Earth Science & Engineering, Imperial College, London, SW7 2BP, United Kingdom*

[2]*Department of Earth Science, University of Bergen, Allégaten 41, 5007 Bergen, Norway*

[3]*WesternGeco Schlumberger, Schlumberger House, Gatwick Airport, Horley, West Sussex, RH6 0NZ, United Kingdom*

§Corresponding author email: c.rodriguez11@imperial.ac.uk

Abstract

Salt dissolution occurs when evaporite-dominated rocks come into contact with NaCl-undersaturated fluids. Salt dissolution can positivity and negatively impact hydrocarbon and mineral exploration, seismic imaging, drilling, and structural restorations in salt-bearing sedimentary basins. However, due to typically poor seismic imaging and a lack of borehole data, few studies have analysed the detailed morphology of salt dissolution-related features (i.e., salt karst) and how this relates to intrasalt stratigraphic heterogeneity, and associated deformation within post-salt overburden. Here we integrate high-quality 3D seismic reflection data, a regional 2D seismic reflection line, and borehole data from the Santos Basin, offshore Brazil to characterise salt dissolution-related features at the crest of buried salt diapirs.

We recognise: (i) flat (<10◦), halite-dominated crests mainly characterised by up to 100 m tall, sub-circular mounds, likely comprising insoluble evaporite; (ii) rugose, evaporite-interbedded crests mainly characterised by up to 100 m deep, oval-to-circular sinkholes above more soluble evaporite units; and (iii) up to 60 m tall breccia pipes, capped by collapse-related sinkholes within the overburden above the flat and rugose crests. Reverse-basin modelling suggests salt dissolution occurred in a fully submarine environment in water depths of 1900 m (± 100 m), which, in combination with seismic-stratigraphic-relationships in post-salt strata, suggests dissolution occurred due to (i) superjacent NaCl-undersaturated seawater which penetrated exposed, thin (up to 60 m) overburden; and (ii) lateral updip migration of formation fluids from flanking submarine channels and lobes. We are therefore able to demonstrate a direct link between the intrasalt stratigraphic heterogeneity, and the style of salt karst, and related deformation in post-salt sedimentary overburden, providing evidence for widespread dissolution of salt in a fully submarine environment.

1. Introduction

Salt (i.e. rocks comprised of soluble minerals that precipitate from the evaporation of brines) is typically dissolved when it comes into contact with NaCl-undersaturated waters. Salt composition varies hence its solubility; i.e., the most soluble and weaker evaporite minerals are the bittern salts (K and Mg salts, e.g., carnallite, tachyhydrite) followed by halite (NaCl), whereas the least soluble are anhydrite and gypsum (e.g.; Warren, 2006). Hence, when salt dissolution occurs, the more-soluble evaporites

(bitterns and halite) are dissolved first, resulting in the body becoming relatively enriched in anhydrite and other insoluble intrasalt residue. Prolonged contact with undersaturated fluids may lead to rehydration of anhydrite and the formation of gypsum, a process particularly common in caprock formed at the top of diapirs (e.g. Jackson et al. 1990; Hovorka, 2000; Warren, 2006). In addition, anaerobic microbial activity within caprocks can lead to the deposition of thick calcium carbonate- and sulphite-rich units (e.g.; Kyle and Posey, 1991; Jackson and Hudec, 2017).

Subaerial dissolution of salt has been extensively studied, indicating this process typically results in: (i) discordant geometrical relationships between remaining salt and overburden, (ii) the formation of a residual caprock or diapiric solution breccias, (iii) the development of salt karst features, such as sinkholes, grooves, caves, and residual mounds; and (iv) overburden deformation (e.g.; Jackson et al., 1990; Warren, 1997; Cartwright et al., 2001; Abelson et al., 2006; Warren, 2006; Bruthans et al., 2009; Hudec et al., 2011; Frumkin, 2013; Gutiérrez and Lizaga, 2016; Jackson and Hudec, 2017). Salt karst identified in Iran resemble those related to subterranean karstic dissolution of calcium carbonate, which have been imaged by seismic data and studied due to the importance of carbonate rocks as hydrocarbon reservoirs (e.g. Evans et al., 1994; Vahrenkamp et al., 2004; Sullivan et al. 2006; Zeng et al., 2011; Burberry et al., 2016). However, salt dissolution is not restricted to the subaerial realm, occurring also in submarine settings (e.g., Bertoni and Cartwright, 2005; Talbot and Augustin, 2016). For example, in the Orca Basin, Gulf of Mexico a salt body is currently exposed at the seabed and is currently being dissolved by NaCl-undersaturated seawater, producing brines that flow downslope into an enclosed submarine brine lake (Shokes et al., 1977;

Tompkins and Shephard, 1979; Pilcher and Blumstein, 2007). Large-scale, likely submarine dissolution of salt has also been inferred for flat- and rugose-topped diapirs imaged in seismic reflection data in the Barents Sea (e.g. Koyi et al. 1995) and in the Netherlands (e.g. Duin, 2001), although the detailed geometry of salt karst and overburden deformation features in both these examples remain unknown.

Identifying salt dissolution and characterising the range of related structural styles has a range of important implications and applications. First, the less-soluble residual evaporite rocks at the crest of dissolved salt structures (i.e, caprock) are the source of economic minerals and have the potential to become reservoir rocks (e.g., Posey and Kyle, 1988; Kyle, 1999). Salt dissolution and related faulting may also generate local accommodation in diapir overburden, potentially promoting reservoir deposition and trap development (e.g., Ge and Jackson, 1998; Cartwright et al., 2001; Hudec et al., 2011; Jackson et al., 2010). In addition, dissolution and related deformation can generate mega-pores and diagenetic alterations, thus reducing the sealing properties of the salt and its overburden, and making it difficult to drill through salt (e.g., Walles, 1993; Black, 1997; Vahrenkamp et al., 2004; Willson and Fredrich, 2005; Jackson and Hudec, 2017). Accurate seismic imaging in salt-bearing sedimentary basins requires a good understanding of caprock stratigraphy and associated seismic velocities variations at the crest and lateral margins of salt structures (e.g., Jackson and Lewis, 2012; Jones and Davison, 2014). Finally, the amount of salt dissolved from the geological record is often unknown, thereby challenging our ability to structurally restore salt-bearing sedimentary basins (e.g, Koyi et al. 1995; Cartwright et al., 2001; Rowan and Ratliff, 2012).

Despite being widespread, and although clearly significant in terms of its impact on resource exploitation, surprisingly few studies have used 3D seismic reflection data to investigate the processes and products of large-scale salt-related dissolution (e.g.; Bertoni and Cartwright, 2005; Pilcher and Blumstein, 2007; Jackson and Lewis, 2012; Burberry et al., 2016; George et al., 2017). This is perhaps surprising given that, despite being unable to resolve sub-decametre structural or stratigraphic details, 3D seismic reflection data do permit relatively detailed characterisation of salt karst-related morphologies and associated overburden deformation over very large areas and for several structures. When coupled with borehole data, seismic expression can be correlated to salt and overburden, which can in turn be related to observed dissolution structural style. A subsurface-based approach, drawing on 3D seismic reflection and borehole data can thus compliment other, principally 1D (e.g. borehole) to quasi-3D (i.e. field) approaches.

The aims of our study are to; (i) characterise the style of intra- and supra-salt, dissolution-related deformation; (ii) relate deformation style to intrasalt stratigraphic heterogeneity, (iii) understand the mechanisms driving salt dissolution; and (iv) determine whether dissolution was submarine or subaerial, and to critically discuss what this means for the regional geodynamic evolution of the study area. To achieve these aims we integrate high-quality 3D seismic reflection, 2D seismic and borehole data from the Santos Basin, offshore Brazil, focusing on six, very well-imaged diapirs. This is an ideal location to characterise salt karst and overburden morphology, given the relatively shallow burial depth (<1000 m) of the studied diapirs and resultant excellent

seismic reflection imaging. Furthermore, borehole data and highly reflective intra-salt layers allow salt karst style to be related to intrasalt stratigraphic heterogeneity.

2. Geological setting

The Santos Basin is located in eastern offshore Brazil and originated as a result of the opening of the South Atlantic Ocean between east South America and West Africa (Fig. 1). During the Barremian, non-marine to shallow marine sediments were deposited within rift basins formed due to continental stretching (Fig. 2; e.g., Demercian, 1996; Meisling et al., 2001; Gomes et al., 2002; Moreira et al., 2007). An initially isolated and irregular rift-related valley was intermittently flooded by seawater in the Aptian, with subsequent dessication events leading to deposition of a regionally extensive, up 2.5 km thick, evaporite-dominated sequence (i.e., Ariri Formation; e.g., Szatmari 2000; Dias 2004; Davison 2007; Karner and Gambôa, 2007; Davison et al., 2012; Rodriguez et al. (a) in press). Subsequent Albian widening and deepening of the proto-south Atlantic Ocean promoted deposition of a shallow-marine carbonate platform in proximal areas and marls in distal areas (Fig. 2; Moreira et al., 2007). Fully marine conditions became established in the Late Cretaceous, following drowning of the Albian carbonate platform. Subsequent uplift and south-eastwards tilting of this segment of the Brazilian margin drove south-eastwards progradation of a thick, clastic-dominated wedge (Fig. 2, e.g. Modica and Brush, 2004; Moreira et al., 2007).

From the Turonian to the Paleocene, deep-water systems were initially deposited within a large, salt-controlled, intra-slope depocenter called the ‘Albian Gap’, before spilling

136 further south-eastwards into numerous smaller minibasins (e.g. Rodriguez et al.(b) in
137 press). Subsequent onshore uplift and diversion of the Paraiba do Sul river to the NE
138 during the Eocene resulted in relatively limited sediment supply to the Santos Basin,
139 with deposition dominated by suspension settling of very fine-grained clastics and
140 carbonates, and emplacement of shelf- and salt-sourced mass transport complexes
141 (MTCs) (e.g., Cobbold et al., 2001; Modica and Brush, 2004; Guerra and Underhill, 2012;
142 Rodriguez et al.(b) in press). Apart a few, albeit large, shelf-sourced MTCs (e.g., Jackson
143 2011; Rodriguez et al.(b), in press), post-Eocene deposition in the central deepwater
144 Santos Basin dominated by very fine-grained sediment (Fig. 2; Modica and Brush, 2004;
145 Moreira et al., 2007; Guerra and Underhill, 2012).

146

147 3. Dataset

148 We use a high-quality 3D time-migrated seismic reflection volume (provided by CGG), a
149 2D post-stack depth-migrated seismic that intersects the 3D volume (provided by
150 WesternGeco), and data from eight publicly available boreholes (Fig. 1b). Borehole data
151 are sparse across the study area, containing only cutting-derived lithology information,
152 and formation markers for the presalt, the intrasalt and postsalt sequences. Two of the
153 boreholes contain a comprehensive set of electrical logs for the intrasalt (eg. GR,
154 Neutron, Density and P-Sonic), and these allow us to tie seismic and borehole data, and
155 to assign lithology information to the mapped intervals (Fig. 2a).

156 The 2D depth seismic profile is c. 350 km long and has a record length of 16 km,
157 providing a good quality regional image along the central deep-water Santos Basin (Fig.

158 2b). The high-quality 3D seismic reflection volume covers an area of 20,122 km^2 and
159 contains trace data from the sea level down to 5.5 seconds two-way time (TWT). The 3D
160 dataset has a vertical sample rate of 4 ms, inline spacing (east-west) of 18.75 m and
161 crossline spacing (north-south) of 25 m. The stratigraphic units of interest (i.e.; unit 3,
162 unit 4 and the intrasalt within the crests of salt walls; Fig. 2a) lie between 3.2-3.6 s TWT
163 interval of the 3D seismic data. The dominant frequency varies with depth but it is c. 40
164 Hz in unit 3 and unit 4 and c. 37 Hz in the intrasalt units near the crest of the salt walls.
165 The vertical seismic resolution within these units is estimated to be 12 m and 30 m,
166 based on average interval velocities of 1900 m s^{-1} for the shallowly buried overburden
167 and 4500 m s^{-1} for the salt. The interval velocities used for the stratigraphic units of
168 interest are averages, based on checkshot data from boreholes 532A, 723C and 709 (Fig.
169 1b). Regional seismic profiles from 2D and 3D data are displayed with SEG normal
170 polarity, where a downward increase in acoustic impedance is represented by a positive
171 reflection event (black) and a downward decrease in acoustic impedance is represented
172 by a negative reflection event (red). Local seismic profiles from 3D data, which illustrate
173 detailed salt karst features, are also displayed with SEG normal polarity although, in
174 these images, a positive reflection event is red and a negative reflection event is blue.

175

176 4. Methods

177 We mapped eight key regional horizons in depth along the 2D seismic profile (Fig. 2b).
178 We mapped these horizons, excluding Basement, but including three additional intrasalt
179 horizons imaged near the diapir crests, in the 3D seismic volume in TWT (top A1, top A2

and top A3; Figs. 2a; 3a). A synthetic seismogram provides a tie between lithology and seismic expression for the intrasalt stratigraphy and the Top Salt (boreholes 709 and 532A; Figs. 3a, 3b; see also Jackson et al. 2015b and Rodriguez et al.(a) in press). For the post-salt stratigraphy, ages and lithology were assigned to seismic horizons based on regional studies and major lithological breaks or unconformities identified in borehole 723C (Fig. 3c; Modica and Brush, 2004; Contreras et al.; 2010; Guerra and Underhill, 2012). For the detailed analysis at the crests of salt diapirs, high-resolution (i.e.; seismic grid spacing of 18.75 m x 25 m) structural maps were generated for the Top Salt and overburden horizons.

We use several seismic attributes to aid our analysis: (1) *amplitude contrast* – this involves calculation of amplitude derivatives between neighbouring traces (Schlumberger, 2012), and we use it here mainly in map-view to highlight structural discontinuities along top salt; (2) *chaos* – this recognises disorganized seismic traces within a 3D window (Randen and Sønneland, 2005), and we use it here mainly in map/plan-view? to investigate and map intra-salt facies variations subcropping top salt; and (3) *sweetness* - this integrates amplitude strength (envelope) and instantaneous frequency (Hart, 2008), and we use it here mainly to highlight cross-sectional variations in seismic facies along the crest of salt walls, and between and within key intrasalt intervals.

We conduct reverse-basin modelling or 'backstripping' of a 2D regional seismic profile to estimate the paleo-water depths at the time of which dissolution likely occurred (i.e. Paleocene; see below) (for general discussion of approach and application in rift basins, see Roberts et al., 2009 and Bell et al., 2014). More specifically, this technique allows us

to assess if dissolution occurred in the subaerial or submarine realm. We justify our application of an overburden-focused, reverse-basin modelling technique (rather than a full kinematic restoration of the salt) for the following reasons: (i) salt movement was likely minimal during and after salt dissolution (i.e., Palaeocene); i.e. we are not attempting to reconstruct the main phases of salt-related deformation, which largely occurred prior to dissolution, during the Albian to Maastrichtian (e.g.; Modica and Brush, 2004; Jackson et al., 2014, 2015; Rodriguez et al.(b) in press); and (ii) only very limited thickness variations occur within post-salt sedimentary overburden capping flat-topped diapirs, again suggesting limited large-scale, syn- to post-dissolution salt movement (Fig. 2c). Reverse reverse-basin modelling technique involves removing: (1) the effect of sediment load and (2) the effect of post-rift thermal subsidence of each of the sedimentary layers in the overburden until the horizon of interest is reached. The removal of each sedimentary layer results in the decompaction of the remaining layers allowing the basin geometry at the time at which the horizon of interest was deposited to be resolved.

A summary of reverse-basin modelling input parameters is shown in Table 1. Lithology information is mainly based on the final well reports available and based on the integration with seismic stratigraphy and seismic attribute analysis by Rodriguez et al.(b), in press (Figs. 2c, 3c; Table 1). A key input parameter in modelling of this type is the effective elastic thickness (T_e), a parameter expressing the strength of the lithosphere (Watts, 1992). In this study, we use a T_e of 5 km, which is representative of the Santos Basin's thinned and thus relatively weak crust, above which loads are supported only locally, over relatively short wavelengths (i.e. Airy isostasy; e.g., Davison

et al.; 2012). Another key input parameter is the beta stretching factor (β), for which we have used a range of values constrained by the 'minimum' and 'maximum' profiles presented by Scotchman et al. (2006). The minimum profile presented by Scotchman et al. (2006) assumes that base salt subsidence from Aptian to the Holocene is due to both syn-rift and post-rift subsidence. Conversely, the maximum profile was calculated assuming that base salt subsidence over the same period occurred due to post-rift thermal subsidence only (Scotchman et al., 2006, 2010).

5. Salt-related structural domains

Before we describe the detailed, dissolution-related morphologies at the crests of salt structures, we first describe the broad salt-related structural domains present within the Santos Basin, with a focus on the external shape and internal structure of salt walls.

Our 2D seismic profile illustrates how salt-related deformation in the Santos Basin varies from NW to SE. Overall, we identify six structural domains (Fig. 2 b, c), i.e.; (i) an upslope, extensional domain, characterised by salt rollers and landward- and basinward-dipping, thin-skinned listric faults; (ii) the Albian Gap, a large, intraslope depocenter, which is bound on its downdip side by a large diapir, and which trapped large amounts of sediment during the Cretaceous to Eocene (e.g., Jackson et al. 2015a); (iii) a minibasin domain, characterised by thick (> 2.5 km deep) minibasins overlying thin or welded salt and bounded by up to 20 km-wide salt walls; (iv) the 'Inner São Paulo Fold Belt' (ISPFB; *sensu* Jackson et al. 2015b), which is defined as a zone of salt-cored folds and predominantly landward-dipping thrusts; (v) the São Paulo Plateau

248 (SPP), which is bound on its eastern margin by the 'Outer High', and which defines a
249 broad structural high characterised by a landward-dipping base salt. The SPP is capped
250 by a highly-reflective, up to 2.5 km thick salt sequence and numerous minibasins; and
251 (vi) a deep basin lying east of the Outer High.

252 The Top Salt structural map generated from our 3D seismic interpretation illustrates the
253 present salt-related deformation occurring in the study area (Fig. 4a). We focus on
254 diapirs in the minibasin domain, the ISPFB and the SPP. Based on distinctly different
255 plan-view trends, external morphologies and sizes, we identify two main types of salt
256 diapir. The first type occurs in the minibasin domain and the ISPFB, trend broadly E or N,
257 and are characterised by broadly rounded but, in detailed, somewhat rugose crests (*R-*
258 *west; R-central* or 'Liam'; see *Jackson et al. (2015 b)*; and *R-east*; Figs. 4 a, b). These
259 diapirs are up 10 km wide and 4 km tall. The second type of diapir occurs in the more
260 distal part of the SPP, trend broadly N or NE, and are characterised by strikingly sub-
261 horizontal (<10◦ dip) crests (*F-west*, *F-central*, and *F-east*; Fig. 4 a, c). Note that *F-central*
262 and *F-east* correspond to *Jimi* and *Freddie* of Jackson et al. (2015b). These diapirs are
263 wider (up to 15 km) but not as tall (up to 2.5 km) as the rounded diapirs (Figs. 4b and
264 4c).

265 Despite their relatively simple external morphologies, many diapirs display considerably
266 greater internal structural complexity (e.g., Davison et al., 2012; Fiduk and Rowan, 2012;
267 Jackson et al., 2014a, 2015b). Of particular interest for this study is the contrast in
268 intrasalt structural style between the flat-topped diapirs, the upper parts of which are
269 invariably dominated by poorly-reflective, intra-salt sheets (Fig. 4c, e.g., Jackson et al.
270 2014a, 2015b), and the rounded salt diapirs, which may locally contain intra-salt sheets

(e.g. *R-east* in Fig. 4b), but which may also contain reverse shear zones and internal anticlines (*R-west* and *R-central* in Fig 4b, see also Jackson et al., 2015b). This structural and associated compositional variability is important when we later consider the style of salt dissolution and its relationship with subcropping intrasalt stratigraphy (see below).

6. Intrasalt and postsalt stratigraphy

Seismic data show that the top of the Aptian salt is characterised by a high-amplitude and broadly continuous seismic event, reflecting the large acoustic impedance contrast between the relatively high-velocity salt and lower velocity, non-evaporitic overburden (Figs. 3b, 4b, c). Boreholes penetrating the salt indicate Top Salt correlates with a 12-56 m thick anhydrite (Fig. 3b). Along the crests of rounded, rugose diapirs, Top Salt exhibits a discordant stratigraphic relationship with highly reflective, anhydrite-halite-carnallite-interbedded, A2 and low-to-moderate-amplitude, relatively halite-rich A3 (Table 2; Fig. 4b). Conversely, Top Salt overlies poorly reflective, halite-rich, A1-allochtonous sheets at the crests of flat-topped diapirs (Table 3; Figs. 4c; see also Jackson et al.; 2015b).

Seismic data show the postsalt sequence in the distal ISPFB and SPP is characterised by low-to-moderate amplitude, continuous seismic reflections, except for Unit 3, which is defined by unconformity-bound wedges composed of moderate-to-high-amplitude, discontinuous to chaotic seismic facies (i.e., Maastrichtian-to-Palaeocene seismic unit on Fig. 4c; see also Rodriguez et al.(b) in press). Above the crests of diapirs, Unit 3 is dominated by low-to-moderate amplitude reflections, although its seismic expression

293 varies between salt diapirs; i.e., conformable continuous sheets, disrupted sheets with
294 apparent downlap, mounded, rotated and chaotic (SF1-SF7; Tables 2 and 3). Boreholes
295 that penetrate the ISPFB and the SPP indicate that the post-salt succession is mostly
296 dominated by fine-grained lithologies, predominantly mudstones and marls (boreholes
297 532A, 723C, 709, 594, Fig. 1b). However, a notable exception occurs on the eastern
298 flank of a distal minibasin in the SPP, where Unit 1 and Unit 3 are characterised by
299 interbedded mudstone, siltstone and sandstone (borehole 723C, Fig. 4c). The salt diapir
300 crests of interest are not penetrated by boreholes. Rodriguez et al.(b), (in press) show
301 that Unit 3 contains sandstone-rich channel-levee and lobes complexes, some of which
302 are capped by mudstone-dominated Mass Transport Complexes (MTCs). The channels
303 and lobes within Unit 3 onlap onto and dip away from some of the salt walls in the
304 study area (Fig. 4c; Rodriguez et al.(b), in press).

305

306 # 7. Seismic expression of salt karst

307 Having described the external morphology of the diapir crests, and the stratigraphy and
308 seismic expression of the salt and its overburden, we here use high-resolution top salt
309 structural maps and seismic attributes to describe salt karst features. We also describe
310 the spatial relationship between salt karst features and: (i) underlying variations in
311 intra-salt lithology; and (ii) overburden deformation patterns (Tables 2 and 3).

312

313 ## 7.1 Sinkholes

50 ms TWT deep (c. 100 metres deep) by c. 50 to 500 m diameter, circular to oval-shaped depressions occur along Top Salt (Figs. 5 and 6). The depressions are 'U'- or 'V'-shaped in cross-section, with their margins dipping 60°-90° (Figs. 5 d, e). The bases of the depressions are characterised by lower sweetness attribute values (Fig. 5e) and higher chaos attribute values (Fig. 6e) than otherwise observed along Top Salt, suggesting lateral variations in the composition and structure. Depressions are isolated or clustered (Figs. 5b, 6b). Depressions are best developed along diapirs characterised by rounded crests, typically underlying mounded-to-chaotic overburden (*SF6* and *SF7*), and overlying halite-rich A3 and truncated, dipping, heterogeneous A2 (Table 2*;* Figs. 5d, 6d).

Based on their seismic expression, geometry, scale and occurrence atop a salt-rich unit, we interpret these features as sinkholes or dolines that formed due to dissolution at the diapir crests (cf. Spain; Elorza and Santolalla, 1998; Gutiérrez et al., 2008; Galve et al., 2009; United States; Ege, 1984; Johnson, 2005, 2008). Furthermore, our analysis suggests that variability in top salt subcrop, related to intrasalt structural and stratigraphic variability (*R-west*, *R-central* and *R-east*), led to preferential dissolution and development of sinkholes above the more soluble, halite-rich A3, and dipping, more heterogeneous layers of A2 (Figs. 5d-e, 6d-e). We speculate that sinkholes preferentially develop within the more soluble, halite- and carnallite-rich layers within A2. Irrespective of the precise underlying lithological control on sinkhole formation, it is clear that their development led to deformation of immediately overlying overburden strata (e.g., SF6 and SF7; Table 2).

7.2 Residual mounds

50 ms, TWT (c. 100 metres deep) by 50 m to 500 m in diameter, sub-circular, elongate and irregular mounds occur along the Top Salt (Figs. 7-9). The local positive-relief features are defined by steeply-dipping (c. 70°- 90°) walls and smooth or rugose tops (Figs. 7d, 8c and 9e). We note that, in contrast to the negative-relief sinkholes described above, these features are characterised by high sweetness attribute values along the top salt (Figs. 7e, 8d). In addition, these mounds are bounded by high chaos attribute values, representing discontinuities along the top salt and in the overburden (Fig. 8d). These mounds are most evident where they appear in clusters below semi-continuous to disrupted strata (*SF1, SF2* and *SF4*) and above poorly-reflective, A1-allocthonous-sheets (e.g., *F-east*, *F-west* and *F-central;* Table 3*;* Figs. 7b, 8b). In addition, some isolated mounds are also found along the rugose crests, overlying poorly-reflective A3 and highly-reflective A2 and underlying mounded-to-chaotic overburden strata (e.g, *SF5*, *R-central*; Fig. 9b, e).

Based on their seismic expression, geometry, scale and occurrence atop a salt-rich unit, we interpret these features as salt dissolution-related karst mounds formed by the insoluble residuum left after dissolution of halite-rich, A1 sheets (e.g., Posey and Kyle, 1988; Warren, 1997; Kyle and Posey, 1991; Hovorka, 2000; Jaworska and Novak, 2013; Jackson and Hudec, 2017). Geometrically similar, gypsum-dominated karst hills or mounds, formed due to near-surface dissolution in the subaerial realm, have been described from other sedimentary basins (e.g., Stafford et al., 2008, Chiesi et al., 2010). We also suggest that the more isolated mounds rising above the crests of rounded-

359 topped diapirs represent the remains of A4 and A3 evaporites dissolved from the cores
360 of intrasalt anticlines (Fig. 9).

361

362 ## 7.3 Breccia pipes

363 60 ms (TWT) (c. 60 metres) tall by c. 30 metres wide, parallel to sub-parallel, linear pipes
364 cross-cut the overburden strata (Fig. 10). The pipes are defined by downward-deflected
365 v-shaped depressions which die-out upwards (Fig. 10b). The lowest downward flexure
366 of the pipes defines apparent downlaps on the Top Salt (SF2, Table 3). The uppermost
367 downward flexure capping the pipes define subcircular to oval-shaped (up to 200 m
368 long, 100 m wide) sinkholes contained within linear (up to 2 km long, 200 m wide)
369 depressions (Fig. 11c). The edges of the linear depressions are defined by high
370 amplitude contrast attribute in plan-form (Fig. 10a). The pipes are characterised by high
371 chaos and relatively low sweetness attribute values across the overburden strata (Figs.
372 10 c, d). These vertical discontinuities are best developed in the strata above *F-central*
373 and in less extent above *F-east*, *F-west and R-west (e.g., Figs. 8d, 10 and 11)*. The
374 sinkholes capping the pipes are locally onlapped by a relatively more continuous seismic
375 event of Paleocene-age (Fig. 11 d). Furthermore, we note that the pipes within the
376 overburden are aligned at depth with steps and seismic facies variations along the Top
377 Salt (e.g., Figs. 8c-e, 10d).

378 Based on their seismic expression, geometry, scale and occurrence in strata overlying
379 salt-rich units, we infer these features are breccia pipes or chimneys formed due to
380 collapse above dissolving diapirs. Geometrically and seismically similar, pipe-like

features, also flanked by downward deflected reflections, are documented in seismic reflection data from other carbonate- and evaporite-bearing basins (e.g. Hardage et al., 1996; Bertoni and Cartwright, 2005; Burberry et al., 2016). We infer pipes in the Santos Basin are likely filled with insoluble, likely non-evaporitic sedimentary material that caved in from the overburden. We can approximately constrain the timing of pipe collapse based on the stratigraphic level at which related deformation terminates, with this approaching suggesting Late-Maastrichtian-to-Paleocene deformation (Fig. 11d). The approximate timing of dissolution-related collapse is also constrained by the horizon onlapping the uppermost sinkholes, which cap the breccia pipes (e.g. Fig. 11d).

8. Subaerial or submarine salt dissolution?

We have provided compelling evidence for salt dissolution at the crest of several diapirs in central deep-water Santos Basin. Furthermore, the spatial relationship between overburden deformation (Tables 2 and 3) and underlying salt karst features (section 7) suggest dissolution was subterranean, and occurred in the Paleocene, under an up to c. 60 m thick overburden of fine-grained strata (e.g., Figs. 8, 10 and 11). However, it is still uncertain if the entire succession was submerged or exposed when dissolution occurred.

Dissolution typically occurs in the subaerial realm (e.g.; the Zechstein salt in the North Sea; Clark et al., 1998; Cartwright et al., 2001 and Texas salt diapirs; Jackson and Seni, 1984, Hudec and Jackson, 2011). If this was the case for the Santos Basin, this would

have major implications for our understanding of the post-rift subsidence profile of the basin, and eustatic sea-level variations during the early Paleogene. More specifically, this would indicate that the crests of the salt diapirs and a thin (c. 60 m) overburden were subaerially exposed in the Paleocene. However, numerous observations suggest that, in the Santos Basin, dissolution occurred in a fully submarine setting. More specifically, the stratigraphic context and analysis presented by previous studies (e.g., Modica and Brush, 2004; Moreira et al., 2007; Contreras et al., 2010; de Melo Garcia et al., 2012; Guerra and Underhill, 2012; Rodriguez et al (b)., in press) provide enough evidence that the Santos Basin was characterised by deep waters at least since the Cenomanian. We here attempt to provide a more precise estimate of water depth by reconstructing the basin to the Paleocene.

Our backstripped profiles are shown on Figures 12 d-g; these satisfy the crustal and sediment key input parameters for the central deep-water Santos Basin discussed in the Methods section and shown in Table 1. We present two restorations, based on the minimum (Fig. 12b) and maximum (Fig. 12c) β estimate profiles provided by Scotchman et al. (2006, 2010). To estimate the paleowater depths at the top of Unit 3, the effect of sediment load and post-rift thermal subsidence during Unit4 and Unit 5 deposition are removed (Fig. 12d-g). The removal of Unit 4 and Unit 5 results in the decompaction of the remaining layers and illustrates the basin geometry at the end of deposition of Unit 3 (Figs. 12 f, g). The restoration to the top Unit 3 (i.e. Paleocene; Fig. 3c) predicts that, regardless of the β factor, the diapirs were submarine when dissolution occurred, with their crests lying in waters depths of 1800-2000 m (*R-west* and *F-west*, Figs. 12 f, g).

9. Discussion

We have provided compelling evidence for fully submarine dissolution of salt at the crest of several diapirs in central deep-water Santos Basin, offshore Brazil. Furthermore, we demonstrate that intrasalt stratigraphic heterogeneity along the salt wall crests controlled salt karst morphology and the associated style of deformation developed within the overburden (section 7). We now discuss the mechanisms that may have triggered salt dissolution, and implications of our findings.

9.1 Mechanism of salt dissolution

Salt dissolution occurs by: (i) descending NaCl-undersaturated fluids, such as freshwater, coming into contact with salt (superjacent dissolution; e.g., Johnson, 1997; Cartwright et al., 2001; Zarei et al.; 2012); (ii) fluids moving laterally through carrier beds in contact with salt (lateral dissolution; e.g.; Ege, 1984; Johnson, 1997; Warren, 1997); or (iii) ascending NaCl-undersaturated fluids, such as connate brines sourced from sub-salt strata, coming into contact with structurally higher salt (subjacent dissolution; e.g., Bertoni and Cartwright. 2005; Jackson and Lewis, 2012; Burberry et al., 2016)

Considering these mechanisms in the context of the Santos Basin example, we suggest that subjacent dissolution, with fluids sourced from subsalt stratigraphy, is unlikely considering the likely impermeable nature of the very tall (>1000 ms, TWT; >2000 m),

447 evaporite-dominated diapirs and the fine-grained-dominated, flanking minibasins (Fig. 4
448 b, c). Although clastics and carbonates are present within the salt, it is in only small
449 proportions and they are likely left in welds (e.g.; Jackson et al. 2014b). Therefore, we
450 infer that dissolution of the crests occurred either by superjacent NaCl-undersaturated
451 seawater or by fluids that migrated laterally from carrier beds directly in contact with
452 the salt.

453 We therefore propose that superjacent dissolution is the only feasible mechanism for
454 driving widespread salt dissolution in the central deep-water Santos Basin during the
455 Paleocene, and in a fully submarine setting. Similar to that occurring in the Orca Basin,
456 northern Gulf of Mexico (Pilcher and Blumstein, 2007), NaCl-undersaturated seawater
457 would have penetrated the very fine-grained, but unlithified and thus highly permeable
458 overburden, driving dissolution of diapir crests. We suggest that subsequent
459 overburden deformation via fracturing, driven by underlying salt depletion, increased
460 permeability and facilitated the further ingress of NaCl-undersaturated seawater,
461 driving to more salt dissolution (Fig. 13a).

462 Considering the Paleocene age of salt dissolution, and the composition and geometry of
463 the post-salt sedimentary overburden (section 9; Figs. 13), we suggest that lateral
464 dissolution, by the migration of fluids from sandstone-rich channels directly in contact
465 with the salt, may also have contributed, locally, to salt dissolution (Fig. 13b). More
466 specifically, we infer that formation fluids may have flowed from the minibasin flanks
467 towards the diapirs crests via sandstone-rich, deepwater turbidites (Fig. 13b).
468 Furthermore, we propose that this mechanism likely promoted the dissolution of the *F-*
469 *central* and *F-west* salt walls, which are both flanked by deep-water channels and lobes.

For example, we interpret that formation fluids within the sandstone-rich channels onlapping the crest of *F-central* became in contact with the A1-halite-rich crests and led to depletion, subsidence and the formation of salt karst atop the crest. We further propose three likely mechanisms that occur isolated or in conjunction, triggering the dewatering of the submarine channels and lobes and the migration of fluids towards the crest: i) initial compaction of the sand-rich submarine channels and lobes (cf. West Africa, Pilcher and Argent, 2007); (ii) coeval salt movement which caused rotation of the channels and levees during deposition (see Rodriguez et al. (b), in press); or (iii) a regional basin-scale event associated to the deposition of mass transport complexes (MTCs) in the Palaeocene and leading to the escape of overpressure fluids.

This dissolution mechanism could also explain the variations in the magnitude and style of dissolution between the crests of flat-topped salt walls. For example, we observe that *F-west* seem to have dissolved more relative to *F-east* given the larger number of thicker and widespread karst mounds forming the highly-reflective caprock (compare Fig.7 with 8). Related to this, we note that submarine channels and lobes within Unit 3 occur on both sides of the highly-dissolved crest of *F-west (Rodriguez et al*. b; in press). Moreover, *F-central* shows more depletion of the evaporite-dominate crest adjacent to the flanking submarine channel (Fig. 11). Conversely, submarine channels are not observed at seismic scale next to *F-east*; suggesting that superjacent dissolution by NaCl-undersaturated seawater may have caused the relatively lower magnitude dissolution observed at its crest.

9.2 Implication of salt dissolution for petroleum systems development

Salt may represent a seal or a reservoir, and salt-related deformation may generate traps. A key challenge when understanding reservoir compartment into salt is characterising the size, continuity, connectivity of collape-related features, largely due to poor sesmic imaging and sparse wells. We here show that salt dissolution can significantly influence the structure of overburden strata (section 7). In this study, we illustrate a variety of reflection configurations within strata above dissolved salt walls, which are strongly dependent of the underlying intrasalt stratigraphy, the timing of deposition relative to dissolution and the magnitude of underlying salt-related dissolution (Tables 2 and 3). For example, we show that the dissolution of evaporites-interbedded salt crests can result in the truncation of the intrasalt stratigraphy and the formation, above, of residual less-soluble caprock that can sometimes preserve the dipping of underlying intrasalt units (Table 3; Fig. 13). The complex reflection configurations and the composition of the overburden can be highly variable comprising a combination of less-soluble residual evaporites combined with sediments collapse from the overburden during subterranean salt depletion (Fig. 13c).

10. Conclusions

The integration of 2D and 3D seismic reflection and borehole data has revealed evidence of submarine salt dissolution in the Santos Basin, offshore Brazil:

1. Seismic stratigraphy and seismic attribute analysis illustrate salt karst features at the crests of salt diapirs consisting of: (i) up to 100 m thick, sub-circular, residual mounds rising above nearly horizontal (<10◦) Top Salt; (ii) up to 100 m deep, oval-to-

circular, dissolution sinkholes below the main level of the Top Salt; and (iii) up to 60 m tall breccia pipes capped by collapse sinkholes within the overburden. Styles of dissolution identified suggest a direct link between the salt karst morphologies and the intrasalt stratigraphic heterogeneity along the top salt.

2. Seismic-stratigraphic-relationships in post-salt strata indicate several deformation patterns within the overburden; from local disruption of conformable sheets, rotation and apparent downlap, mounds and highly chaotic. The magnitude of deformation within the overburden is controlled by the magnitude of dissolution of the underlying evaporite-dominated crests; thus, indicating subterranean salt dissolution.
3. Reverse-basin modelling indicates that salt dissolution occurred in a fully submarine environment in water depths of 1900 m (± 100 m).
4. Widespread dissolution occurred due to NaCl undersaturated seawater during partial salt diapir exposure (under an up 60 m thick, fine-grained dominated overburden) at the seabed; and locally, due to (ii) dissolution by formation fluids migrating from Late-Maastrichtian-to-Paleocene submarine channels and lobes directly in contact with the salt-dominated crests.
5. Results presented in this study has direct implications for reservoir characterisation and sealing capacity of the crests of salt diapirs and its overburden.

11. Acknowledgments

We would like to thank CGG for providing access to the 3D seismic data and for granting permission to publish the results of this study. We also thank Statoil and ANP Brazil for

providing access to the borehole data. Schlumberger WesternGeco is also gratefully acknowledged for providing 2D seismic regional data, partial funding and support of this work.

12. Figure captions

FIGURE 1: (a) Eastern Brazil salt-dominated sedimentary basins highlighting the location of the Santos Basin, offshore Brazil; (b) Study area in the central deep-water Santos Basin. Location of 2D seismic profile, 3D seismic reflection and borehole data available for the study.

FIGURE 2: (a) Seismic stratigraphic framework; key intrasalt stratigraphic intervals A1-A4 for this and previous studies (Jackson et al., 2014, 2015; Rodriguez et al.(a) in press). B1, B2 and B3 refer to competent layers or 'beams' defined by high amplitude continuous reflections. D1, D2 and D3 refer to ductile detachment zones defined by acoustically transparent, poorly continuous reflections (Fiduk and Rowan, 2012). (b) 2D depth seismic profile illustrating salt-related structural domains in the Santos Basin. (c) Geoseismic profile with interpreted seismic units.

FIGURE 3: (a) Borehole (709) and seismic expression for the intrasalt stratigraphy. A1-A4 intrasalt key stratigraphic intervals are defined by vertical variations in seismic facies and the integration with borehole data. Intrasalt lithology was identified based on the typical well log response for evaporites for a combination of wireline logs; i.e., density (RHOB), sonic (DT), neutron porosity (NPHI) and gamma-ray (GR) (see also. Jackson et al., 2015; Rodriguez et al., in press); (b) Borehole (532A) and seismic expression of the Top Salt in a structurally-low and relatively undeformed area; (c) Borehole (723C) and

561 seismic expression of the post-salt sedimentary overburden. Key post-salt seismic units
562 are defined based on vertical variations in seismic facies and the integration with
563 borehole data.

564 **FIGURE 4**: (a) Top salt structural map with locations of salt walls of interest; (b) Seismic
565 section across salt diapirs with rounded and rugose crests; (c) Seismic section across salt
566 diapirs with flat crests.

567 **FIGURE 5**: Seismic expression of salt dissolution-related sinkholes: (a) R-west top salt
568 structural map; (b) Salt karst along Top Salt and intrasalt stratigraphy subcropping the R-
569 west salt diapir; (c) Amplitude contrast attribute map for R-west Top Salt highlighting
570 the sinkholes along Top Salt, see Figure 5a for location; (d) Seismic section along the
571 crest of R-east illustrating the geometry of sinkholes (indicated by white arrows) and
572 their relationship to halite-rich A3 intrasalt unit. Location is shown on Figure 5c; (e)
573 Sweetness attribute of the seismic section on (d).

574 **FIGURE 6**: Seismic expression of salt dissolution-related sinkholes: (a) R-east top salt
575 structural map; (b) Salt karst along Top Salt and Intrasalt stratigraphy subcropping R-
576 east salt diapir; (c) Amplitude contrast attribute map for R-east Top Salt highlighting the
577 sinkholes along Top Salt, see Figure 6a for location; (d) Seismic section along the crest of
578 R-east illustrating the geometry of sinkholes (indicated by white arrows) and their
579 relationship to dipping-A2 intrasalt stratigraphy. Location is shown on Figure 6c; (e)
580 Chaos attribute of the seismic section on Figure 6d highlighting the sinkholes along the
581 Top Salt.

582 **FIGURE 7:** Seismic expression of residual mounds: (a) F-east top salt structural map; (b)
583 Intrasalt unit subcropping F-east salt diapir; (c) Amplitude contrast attribute map for F-

east Top Salt highlighting residual mounds above the nearly-horizontal Top Salt; (d) Seismic section along the crest of F-east illustrating residual mounds above the main top salt level (mounds are indicated by white arrows). See Figure 7c for location; (e) Sweetness attribute for section on Figure 7d highlighting potential facies variations along the Top Salt.

FIGURE 8: Seismic expression of residual mounds: (a) F-west Top Salt structural map; (b) Salt karst along Top Salt and intrasalt stratigraphy subcropping F-west Top Salt; (c) Seismic section along the crest of F-west illustrating residual mounds defined by highly-reflective packages along the Top Salt (mounds are indicated by white arrows). See location on (a) and (b); (d) Chaos attribute for the seismic section on (c) highlighting the discontinuities along the Top Salt and within the overburden; (e) Sweetness attribute for section on (a) illustrating the facies variations along Top Salt and within the mounds.

FIGURE 9: Seismic expression of residual mounds: (a) R-central Top Salt structural map; (b) Salt karst morphology and intrasalt stratigraphy subcropping R-central Top Salt; (c) Zoom into Top Salt structural map highlighting the location of the residual mounds; (d) Amplitude contrast map of 8 c; (d) Seismic section across mounds on R-Central salt diapir illustrating remnant mounds after A4 and A3 dissolution. See (c) and (d) for location.

FIGURE 10: Seismic expression of breccia pipes or chimneys within the overburden: (a) Amplitude contrast seismic attribute time slice highlighting the edges of the breccia pipes. See location on Figure 11a; (b) Seismic section accross the crest of F-central and overburden strata. Breccia Pipes are indicated with white arrows; (c) Chaos seismic attribute for the section on Figure 10b highlighting the breccias cross-cutting the

overburden strata; (d) Sweetness seismic attribute for the section on Figure 10b. Some of the breccia pipes correlate with facies variations along the Top Salt.

FIGURE 11: (a) F-central Top Salt structural map; (b) Salt karst morphology and intrasalt stratigraphy along the crest of F-central; (c) Structural map for the seismic horizon within the overburden (blue on (d)) highlighting the collapse associated to dissolution of the underlaying halite-rich crest and the top of a channel flanking the salt wall; (d) Seismic section across F-central and the flanking minibasin illustrating the onlap of the channel and discontinuities within the overburden.

FIGURE 12: (a) Input model used for basin restoration based on the interpretation of 2D depth seismic profile (Figure 2b). See Key on Figure 2a; (b) Minimum Beta Stretching Factor along the 2D seismic profile (after Scotchman et al., 2006); (c) Maximum Beta Stretching Factor along the 2D seismic profile (after Scotchman et al., 2006); (d) Basin restoration to the mid-Oligocene (28 Ma) based on the minimum Beta Stretching Factor profile; (e) Basin restoration to the mid-Oligocene (28 Ma) based on the maximum Beta Stretching Factor profile; (f) Basin restoration to the Paleocene (60 Ma) based on the minimum Beta Stretching Factor profile; (f) Basin restoration to the Paleocene (60 Ma) based on the maximum Beta Stretching Factor profile

FIGURE 13: Mechanisms and styles of submarine salt dissolution: (a) Superjacent dissolution by NaCl-undersaturated seawater penetrating the very fine-grained, unlithified overburden during exposure at the seafloor; (b) Dissolution due to fluids migrating from carrier beds directly in contact with the salt; (c) Residual Solution breccia formed by the preferential depletion of the evaporite-dominated crests and collapse of the overburden.

630

631

632 13. Table captions

633 Table 1: Post-salt sediment key input parameters for the basin restoration based on
634 seismic interpretation and well reports available.

635 Table 2: Overburden seismic expression and thickness variations above dissolved rugose
636 crests.

637 Table 3: Overburden seismic expression and thickness variations above dissolved flat
638 crests.

639

640 14. References

641 Abelson, M., Yechieli, Y., Crouvi, O., Baer, G., Wachs, D., Bein, A. and Shtivelman, V.,
642 2006. Evolution of the Dead Sea sinkholes. Geological Society of America Special Papers,
643 401, pp.241-253.

644 Bell, R.E., Jackson, C., Elliott, G.M., Gawthorpe, R.L., Sharp, I.R. and Michelsen, L., 2014.
645 Insights into the development of major rift-related unconformities from geologically
646 constrained subsidence modelling: Halten Terrace, offshore mid Norway. Basin
647 Research, 26(1), pp.203-224.

Bertoni, C. and Cartwright, J.A., 2005. 3D seismic analysis of circular evaporite dissolution structures, Eastern Mediterranean. Journal of the Geological Society, 162(6), pp.909-926.

Black, T.J., 1997. Evaporite karst of northern lower Michigan. Carbonates and Evaporites, 12(1), p.81.

Burberry, C.M., Jackson, C.A.L. and Chandler, S.R., 2016. Seismic reflection imaging of karst in the Persian Gulf: Implications for the characterization of carbonate reservoirs. AAPG Bulletin, 100(10), pp.1561-1584.

Bruthans, J., M. Filippi, N. Asadi, M. Zare, S. Šlechta, and Z. Churáčková, 2009, Surficial deposits on salt diapirs (Zagros Mountains and Persian Gulf Platform, Iran): Characterization, evolution, erosion and the influence on landscape morphology. Geomorphology, 107(3), pp: 195-209.

Cartwright, J., Stewart, S. and Clark, J., 2001. Salt dissolution and salt-related deformation of the Forth Approaches Basin, UK North Sea. Marine and Petroleum Geology, 18(6), pp.757-778.

Chiesi, M., J. De Waele, and P. Forti, 2010, Origin and evolution of a salty gypsum/anhydrite karst spring: the case of Poiano (Northern Apennines, Italy). Hydrogeology Journal, 18(5), pp. 1111-1124.

Cobbold, P.R., K.E. Meisling, and V.S. Mount, 2001, Reactivation of an Obliquely Rifted Margin, Campos and Santos Basins, Southeastern Brazil: AAPG Bulletin, v. 85, pp. 1925-1944.

669 Davison, I., 2007, Geology and tectonics of the South Atlantic Brazilian salt basins:
670 Geological Society, London, Special Publications, v. 272, pp. 345-359.

671 Davison, I., L. Anderson, and P. Nuttall, 2012, Salt deposition, loading and gravity
672 drainage in the Campos and Santos salt basins: Geological Society, London, Special
673 Publications, v. 363, p. 159-174.

674 de Melo Garcia, S.F., Letouzey, J., Rudkiewicz, J.L., Danderfer Filho, A. and de Lamotte,
675 D.F., 2012. Structural modeling based on sequential restoration of gravitational salt
676 deformation in the Santos Basin (Brazil). Marine and Petroleum Geology, 35(1), pp.337-
677 353.

678 De Waele, J., Plan, L. and Audra, P., 2009. Recent developments in surface and
679 subsurface karst geomorphology: an introduction.

680 Demercian, L.S., 1996, A halocinese na evolução do Sul da Bacia de Santos do Aptiano
681 ao Cretáceo Superior, MS thesis., p. 201.

682 Dias, J.L. 2004, Tectônica, estratigrafia e sedimentação no Andar Aptiano da margem
683 leste brasileira: Boletim de Geociências da PETROBRAS, v. 13, pp. 7-25.

684 Duin, E., 2001. A detailed 3D seismic interpretation of a salt dome and its caprock, a
685 case study in the northeastern Netherlands. In SEG Technical Program Expanded
686 Abstracts 2001 (pp. 670-673). Society of Exploration Geophysicists.

687 Ege, J.R., 1984. Formation of solution-subsidence sinkholes above salt beds (No. 897).
688 US Geological Survey,.

689 Elorza, M.G. and F.G. Santolalla, 1998, Geomorphology of the Tertiary gypsum
690 formations in the Ebro Depression (Spain). Geoderma, 87(1), pp. 1-29.

691 Evans, M.W., S.W. Snyder, and A.C. Hine, 1994, High-resolution seismic expression of
692 karst evolution within the upper Floridan Aquifer system: Crooked Lake, Polk County,
693 Florida. Journal of Sedimentary Research, 64(2).

694 Fiduk, J. C., and M. G. Rowan, 2012, Analysis of folding and deformation within layered
695 evaporites in Blocks BM-S-8 & -9, Santos Basin, Brazil: Geological Society, London,
696 Special Publications, v. 363, p. 471-487.

697 Friedman, G.M., 1997. Dissolution-collapse breccias and paleokarst resulting from
698 dissolution of evaporite rocks, especially sulfates. Carbonates and Evaporites, 12(1),
699 pp.53-63.

700 Frumkin, A., 1994. Hydrology and denudation rates of halite karst. Journal of Hydrology,
701 162(1-2), pp.171-189.

702 Frumkin, A., 2013. Salt karst. Treatise on geomorphology, 6, pp.407-424.

703 Galve, J. P., F. Gutiérrez, J. Remondo, J. Bonachea, P. Lucha, and A. Cendrero, 2009,
704 Evaluating and comparing methods of sinkhole susceptibility mapping in the Ebro Valley
705 evaporite karst (NE Spain). Geomorphology, 111(3), pp: 160-172.

706 Ge, H. and Jackson, M.P., 1998. Physical modeling of structures formed by salt
707 withdrawal: Implications for deformation caused by salt dissolution. AAPG bulletin,
708 82(2), pp.228-250.

George, M., O.K. Olakunle, J.S. Emil, and P. Abrahamson, 2017, Seismic interpretation and characterization of anhydrite caprocks in the Tromsø Basin, SW Barents Sea. Marine Geology, 390, pp. 36-50.

Gomes, P.O., J. Parry, and W. Martins, 2002, The outer high of the Santos Basin, southern São Paulo Plateau, Brazil: tectonic setting, relation to volcanic events and some comments on hydrocarbon potential: AAPG Hedberg Conference,'Hydrocarbon Habitat of Volcanic Rifted Passive Margins, pp. 8-11.

Guerra, M.C.M., and J.R. Underhill, 2012, Role of halokinesis in controlling structural styles and sediment dispersal in the Santos Basin, offshore Brazil: Geological Society, London, Special Publications, v. 363, pp. 175-206.

Gutiérrez, F., J. Guerrero, and P. Lucha, 2008, A genetic classification of sinkholes illustrated from evaporite paleokarst exposures in Spain. Environmental Geology, 53(5), pp. 993-1006.

Gutiérrez, F. and Lizaga, I., 2016. Sinkholes, collapse structures and large landslides in an active salt dome submerged by a reservoir: The unique case of the Ambal ridge in the Karun River, Zagros Mountains, Iran. Geomorphology, 254, pp.88-103.

Hardage, B.A., D.L. Carr, D.E. Lancaster, J.L. Simmons Jr, R.Y. Elphick, V.M. Pendleton, and R.A. Johns, 1996, 3-D seismic evidence of the effects of carbonate karst collapse on overlying clastic stratigraphy and reservoir compartmentalization. Geophysics, 61(5), pp. 1336-1350.

Hart, B., 2008, Stratigraphically significant attributes: The Leading Edge, v. 27, pp. 320-324.

731 Hovorka, S.D., 2000, Understanding the Process of Salt Dissolution and Subsidence.
732 Solution Mining Research Institute Proceedings.

733 Hudec, M.R., Jackson, M.P., Vendeville, B.C., Schultz-Ela, D.D. and Dooley, T.P., 2011.
734 The salt mine: A digital atlas of salt tectonics.

735 Jackson, C.A., 2011. Three-dimensional seismic analysis of megaclast deformation within
736 a mass transport deposit; implications for debris flow kinematics. Geology, 39(3),
737 pp.203-206.

738 Jackson, C.A., Kane, K.E. and Larsen, E., 2010. Structural evolution of minibasins on the
739 Utsira High, northern North Sea; implications for Jurassic sediment dispersal and
740 reservoir distribution. Petroleum Geoscience, 16(2), pp.105-120.

741 Jackson, C.A.L. and Lewis, M.M., 2012. Origin of an anhydrite sheath encircling a salt
742 diapir and implications for the seismic imaging of steep-sided salt structures, Egersund
743 Basin, Northern North Sea. Journal of the Geological Society, 169(5), pp.593-599.

744 Jackson, C. A.-L., M. P. Jackson, and M. R. Hudec, 2015a, Understanding the kinematics
745 of salt-bearing passive margins: A critical test of competing hypotheses for the origin of
746 the Albian Gap, Santos Basin, offshore Brazil: Geological Society of America Bulletin, v.
747 127, p. 1730-1751.

748 Jackson, C. A.-L., M. P. A. Jackson, M. R. Hudec, and C. Rodriguez, 2014, Internal
749 structure, kinematics, and growth of a salt wall: Insights from 3-D seismic data: Geology,
750 v. 42, p. 307-310.

751 Jackson, C. A. L., M. P. A. Jackson, M. R. Hudec, and C. R. Rodriguez, 2015b, Enigmatic
752 structures within salt walls of the Santos Basin—Part 1: Geometry and kinematics from
753 3D seismic reflection and well data: Journal of Structural Geology, v. 75, p. 135-162.

754 Jackson, M.P.A. and M.R. Hudec, 2017. Salt Tectonics: Principles and Practice.
755 Cambridge University Press. pp. 424-428.

756 Jackson, M.P.A. and Seni, S.J., 1984. The domes of east Texas, pp. 163-179.

757 Jackson, M.P.A., Cornelius, R.R., Craig, C.H., Gansser, A., Stöcklin, J. and Talbot, C.J.,
758 1990. Salt diapirs of the Great Kavir, central Iran. Geological Society of America
759 Memoirs, 177, pp.1-150.

760 Jackson, M.P. and Hudec, M.R., 2016. Salt Tectonics: Principles and Practice. Cambridge
761 University Press.

762 Jaworska, J. and Nowak, M., 2013. Anhydrites from gypsum cap-rock of Zechstein salt
763 diapirs. Geology, Geophysics and Environment, 39(3), pp.233-250.

764 Johnson, K.S., 1997. Evaporite karst in the United States. Carbonates and Evaporites,
765 12(1), pp.2-14.

766 Johnson, K.S., 2005. Subsidence hazards due to evaporite dissolution in the United
767 States. Environ Geol, 48 (3), pp. 395-409.

768 Johnson, K.S., 2008. Evaporite-karst problems and studies in the USA. Environmental
769 Geology, 53(5), pp. 937-943.

770 Jones, I.F. and Davison, I., 2014. Seismic imaging in and around salt bodies.
771 Interpretation, 2(4), pp.SL1-SL20.

772 Karner, G.D. and L.A.P. Gambôa, 2007, Timing and origin of the South Atlantic pre-salt
773 sag basins and their capping evaporites: Geological Society, London, Special
774 Publications, v. 285, pp. 15-35.

775 Koyi, H., Talbot, C.J. and Torudbakken, B.O., 1995. Analogue models of salt diapirs and
776 seismic interpretation in the Nordkapp Basin, Norway. Petroleum geoscience, 1(2),
777 pp.185-192.

778 Koyi, H., 1998. The shaping of salt diapirs. Journal of Structural Geology, 20(4), pp.321-
779 338.

780 Kyle, J.R., 1999. Industrial-Mineral Resources Associated with Salt Domes, Gulf of
781 Mexico Basin, USA. In Proceedings of the 34th Forum on the Geology of Industrial
782 Minerals: Oklahoma Geological Survey, Circular (Vol. 102, pp. 161-178).

783 Kyle, J.R. and H.H. Posey, 1991, Halokinesis, cap rock development, and salt dome
784 mineral resources. Developments in sedimentology, 50, pp. 413-474.

785 Loucks, R.G., 1999. Paleocave carbonate reservoirs: origins, burial-depth modifications,
786 spatial complexity, and reservoir implications. AAPG bulletin, 83(11), pp.1795-1834.

787 Machel, H.G., Borrero, M.L., Dembicki, E., Huebscher, H., Ping, L. and Zhao, Y., 2012. The
788 Grosmont: the world's largest unconventional oil reservoir hosted in carbonate rocks.
789 Geological Society, London, Special Publications, 370(1), pp.49-81.

790 Meisling, K.E., P.R. Cobbold, and V.S. Mount, 2001, Segmentation of an Obliquely Rifted
791 Margin, Campos and Santos Basins, Southeastern Brazil: AAPG Bulletin, v. 85, pp. 1903-
792 1924.

793 Modica, C. J., and E. R. Brush, 2004, Postrift sequence stratigraphy, paleogeography,
794 and fill history of the deep-water Santos Basin, offshore southeast Brazil: AAPG Bulletin,
795 v. 88, p. 923-945.

796 Moreira, J. L. P., C. Madeira, J. A. Gil, and M. A. P. Machado, 2007, Bacia de Santos:
797 Bulletin Geociencias Petrobras, v. 15, p. 531-549.

798 Pilcher, R.S. and Blumstein, R.D., 2007. Brine volume and salt dissolution rates in Orca
799 Basin, northeast Gulf of Mexico. AAPG bulletin, 91(6), pp.823-833.

800 Posey, H.H. and Kyle, J.R., 1988. Fluid-rock interactions in the salt dome environment:
801 an introduction and review. Chemical Geology, 74(1-2), pp.1-24.

802 Randen, T. and Sønneland, L., 2005. Atlas of 3D seismic attributes. In Mathematical
803 Methods and Modelling in Hydrocarbon Exploration and Production (pp. 23-46).
804 Springer Berlin Heidelberg.

805 Roberts, A.M., R.I. Corfield, N.J. Kusznir, S.J., Matthews, E.K. Hansen, and R.J. Hooper,
806 2009. Mapping palaeostructure and palaeobathymetry along the Norwegian Atlantic
807 continental margin: Møre and Vøring basins. Petroleum Geoscience, 15(1), pp. 27-43.

808 Rodriguez, C.R., C.A.L. Jackson, R.E. Bell, A. Rotevatn, and M. Francis, In press (b).
809 Minibasin development and reservoir deposition on a salt-influenced deep-water slope:
810 Santos Basin, offshore Brazil. Accepted by the AAPG Bulletin.

811 Rodriguez, C.R., C.A.L. Jackson, A. Rotevatn, R.E. Bell, and M. Francis, In press (a).
812 Stratigraphy of salt giants: new insights from the Santos Basin, offshore Brazil. Accepted
813 by Geosphere.

814 Rowan, M.G. and Ratliff, R.A., 2012. Cross-section restoration of salt-related
815 deformation: Best practices and potential pitfalls. Journal of Structural Geology, 41,
816 pp.24-37.

817 Schlumberger, 2012, Interpreter's guide to seismic attribuite, 4th edition, pp. 112-114.

818 Scotchman, I.C., Gilchrist, G., Kusznir, N.J., Roberts, A.M. and Fletcher, R., 2010. The
819 breakup of the South Atlantic Ocean: formation of failed spreading axes and blocks of
820 thinned continental crust in the Santos Basin, Brazil and its consequences for petroleum
821 system development. In Geological Society, London, Petroleum Geology Conference
822 series (Vol. 7, No. 1, pp. 855-866). Geological Society of London.

823 Scotchman, I.C., G. Marais-Gilchrist, F.G.D. Souza, F.F. Chaves, L.A. Atterton, A.M.
824 Roberts, and N. J. Kusznir, 2006, A failed sea-floor-spreading centre, Santos Basin, Brazil:
825 Rio Oil & Gas Expo and Conference, Rio de Janeiro.

826 Scott, E., Peel, F., Taylor, C., Bryant, W. and Bean, D., 2001. Deep water Gulf of Mexico
827 sea floor features revealed through 3D seismic. In Offshore Technology Conference.
828 Offshore Technology Conference.

829 Shokes, R.F., Trabant, P.K., Presley, B.J. and Reid, D.F., 1977. Anoxic, hypersaline basin in
830 the northern Gulf of Mexico. Science, 196(4297), pp.1443-1446.

831 Stafford, K.W., R. Nance, L. Rosales-Lagarde, and P.J. Boston, 2008, Epigene and
832 hypogene karst manifestations of the Castile Formation: Eddy County, New Mexico and
833 Culberson County, Texas, USA.

834 Sullivan, E.C., Marfurt, K.J., Lacazette, A. and Ammerman, M., 2006. Application of new
835 seismic attributes to collapse chimneys in the Fort Worth Basin. Geophysics, 71(4),
836 pp.B111-B119.

837 Szatmari, P., 2000, AAPG Memoir 73, Chapter 6: Habitat of Petroleum Along the South
838 Atlantic Margins, pp. 69-75.

839 Talbot, C. and Augustin, N., 2016. Submarine Salt Karst Terrains. AIMS Geosciences,
840 2(2), pp.182-200.

841 Tompkins, R.E. and Shephard, L.E., 1979. Orca Basin: Depositional processes,
842 geotechnical properties and clay mineralogy of Holocene sediments within an anoxic
843 hypersaline basin, northwest Gulf of Mexico. Marine Geology, 33(3-4), pp.221-238.

844 Vahrenkamp, V. C., F. David, P. Duijndam, M. Newall, and P. Crevello, 2004. Growth
845 architecture, faulting, and karstification of a middle Miocene carbonate platform,
846 Luconia Province, offshore Sarawak, Malaysia, in Seismic imaging of carbonate
847 reservoirs and systems: AAPG Memoir 81, p. 329– 350.

848 Walles, F.E., 1993. Tectonic and diagenetically induced seal failure within the south-
849 western Great Bahamas Bank. Marine and petroleum geology, 10(1), pp.14-28.

850 Warren, J.K., 1997. Evaporites, brines and base metals: Fluids, flow and 'the evaporite
851 that was'. Australian Journal of Earth Sciences, 44(2), pp.149-183.

852 Warren, J.K., 2006. Evaporites: sediments, resources and hydrocarbons. Springer
853 Science & Business Media.

854 Watts, A.B., 1992, The effective elastic thickness of the lithosphere and the evolution of
855 foreland basins. Basin Research, 4(3-4), pp. 169-178.

856 Willson, S.M. and J.T. Fredrich, 2005, January. Geomechanics considerations for
857 through-and near-salt well design. In SPE Annual Technical Conference and Exhibition.
858 Society of Petroleum Engineers.pp 1-17.

859 Zarei, M., Raeisi, E. and Talbot, C.J., 2012. Karst development on a mobile substrate:
860 Konarsiah salt extrusion, Iran. Geological Magazine, 149(03), pp.412-422.

861 Zeng, H., Wang, G., Janson, X., Loucks, R., Xia, Y., Xu, L. and Yuan, B., 2011.
862 Characterizing seismic bright spots in deeply buried, Ordovician paleokarst strata,
863 Central Tabei uplift, Tarim Basin, Western China. Geophysics, 76(4), pp.B127-B137.

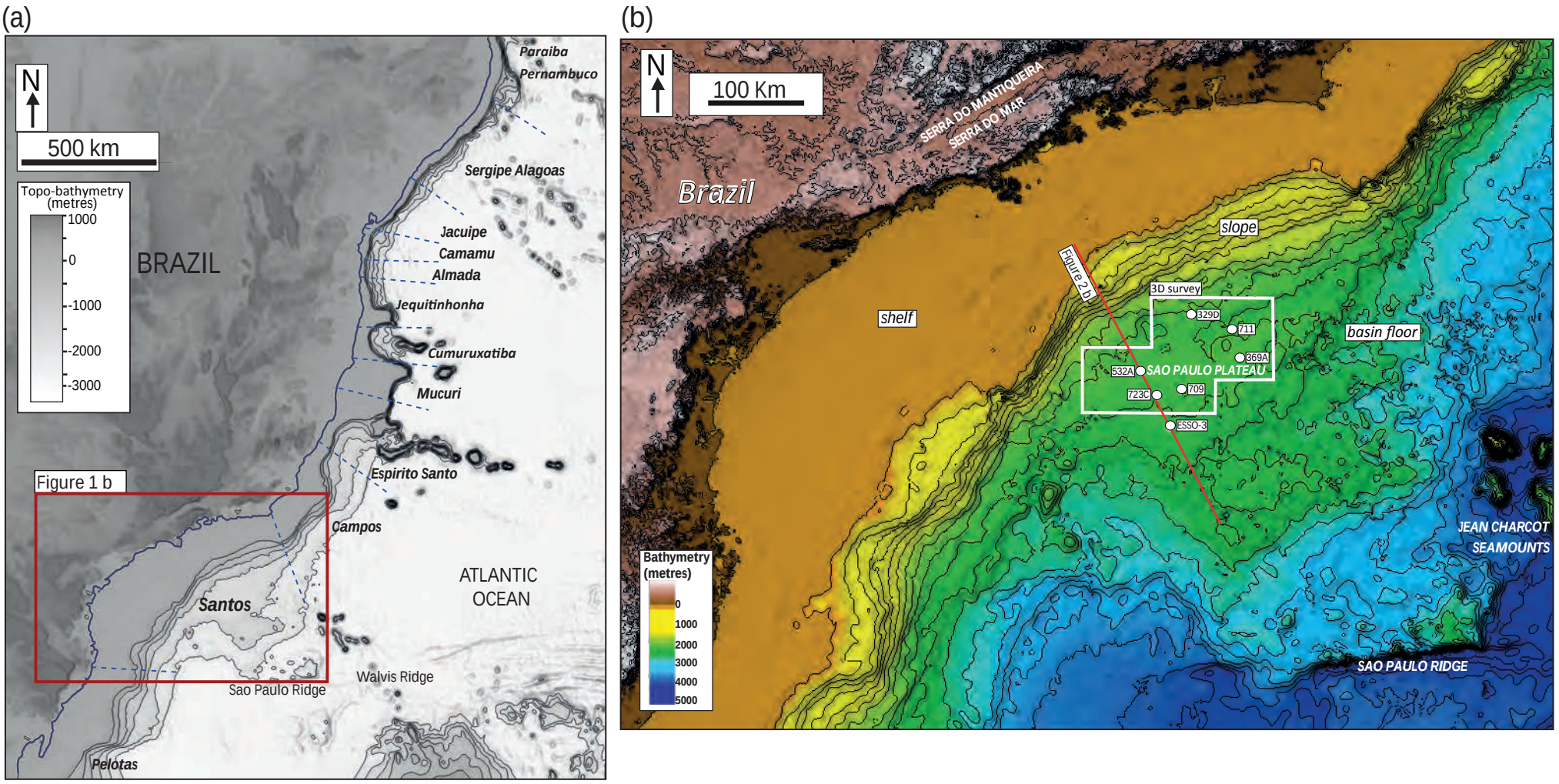

FIGURE 1 (a) Eastern Brazil salt-dominated sedimentary basins highlighting the location of the Santos Basin, offshore Brazil; (b) Study area in the central deep-water Santos Basin. Location of 2D seismic profile, 3D seismic reflection and borehole data available for the study.

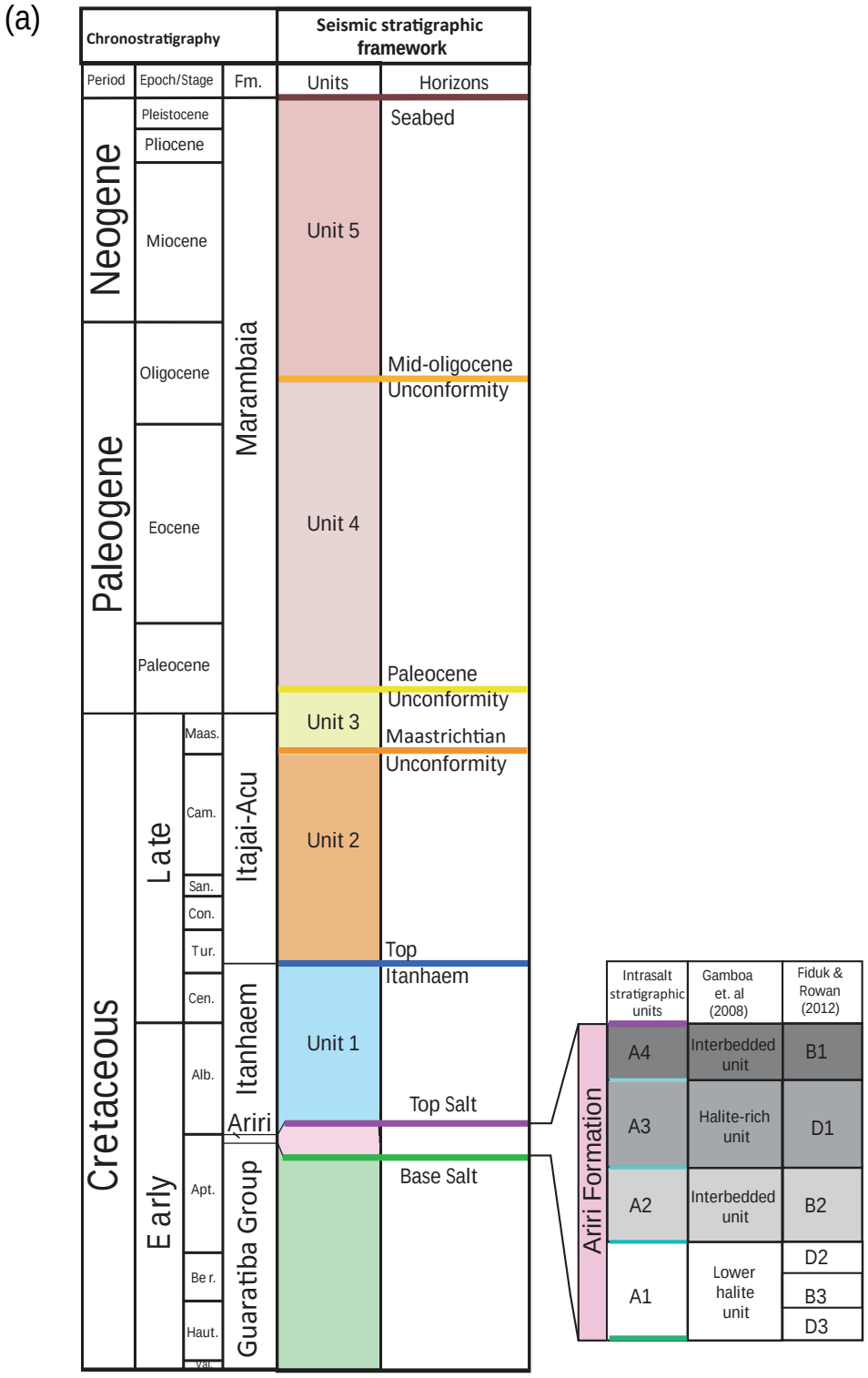

FIGURE 2: (a) Seismic stratigraphic framework; key intrasalt stratigraphic intervals A1-A4 for this and previous studies (Jackson et al., 2014, 2015; Rodriguez et al.(a) in press). B1, B2 and B3 refer to competent layers or 'beams' defined by high amplitude continuous reflections. D1, D2 and D3 refer to ductile detachment zones defined by acoustically transparent, poorly continous reflections (Fiduk and Rowan, 2012). (b) 2D depth seismic profile illustrating salt-related structural domains in the Santos Basin. (c) Geoseismic profile with interpreted seismic units.

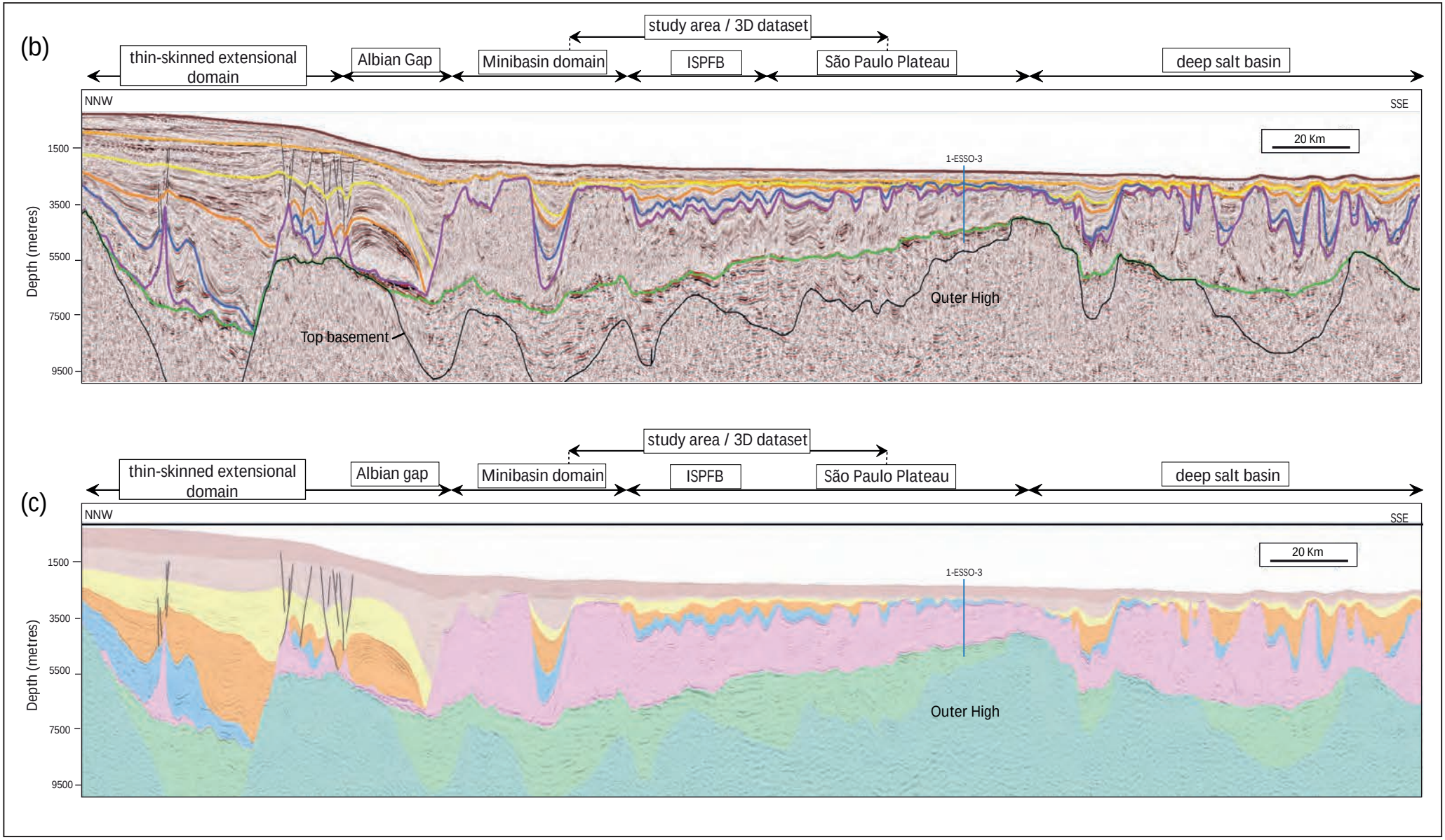
(b)
study area / 3D dataset
thin-skinned extensional domain
Albian Gap
Minibasin domain
ISPFB
São Paulo Plateau
deep salt basin
NNW
SSE
20 Km
1-ESSO-3
Depth (metres)
1500
3500
5500
7500
9500
Top basement
Outer High
(c)
study area / 3D dataset
thin-skinned extensional domain
Albian gap
Minibasin domain
ISPFB
São Paulo Plateau
deep salt basin
NNW
SSE
20 Km
1-ESSO-3
Depth (metres)
1500
3500
5500
7500
9500
Outer High

Table 1: Post-salt sediment key input parameters for the basin restoration based on seismic interpretation and well reports available

Horizon age (Ma)	Horizon name	Unit name	Lithology	Near-surface porosity (%)	Decay constant (1/km)	Matrix density (g/cc)
0	Top Marambaia (Seabed)	Unit 5	90% shale 10%sand	61.6	0.49	2.71
~28	Mid Oligocene Unconformity	Unit 4	80% shale 20%sand	60.2	0.46	2.71
~60	Paleocene unconformity	Unit 3	40% shale 60%sand	54.6	0.37	2.68
~67	Maastrichtian unconformity	Unit 2	60% shale 40%sand	57.4	0.41	2.69
~95	Top Itanhaem	Unit 1	70% shale 30% limestone	65.1	0.57	2.72

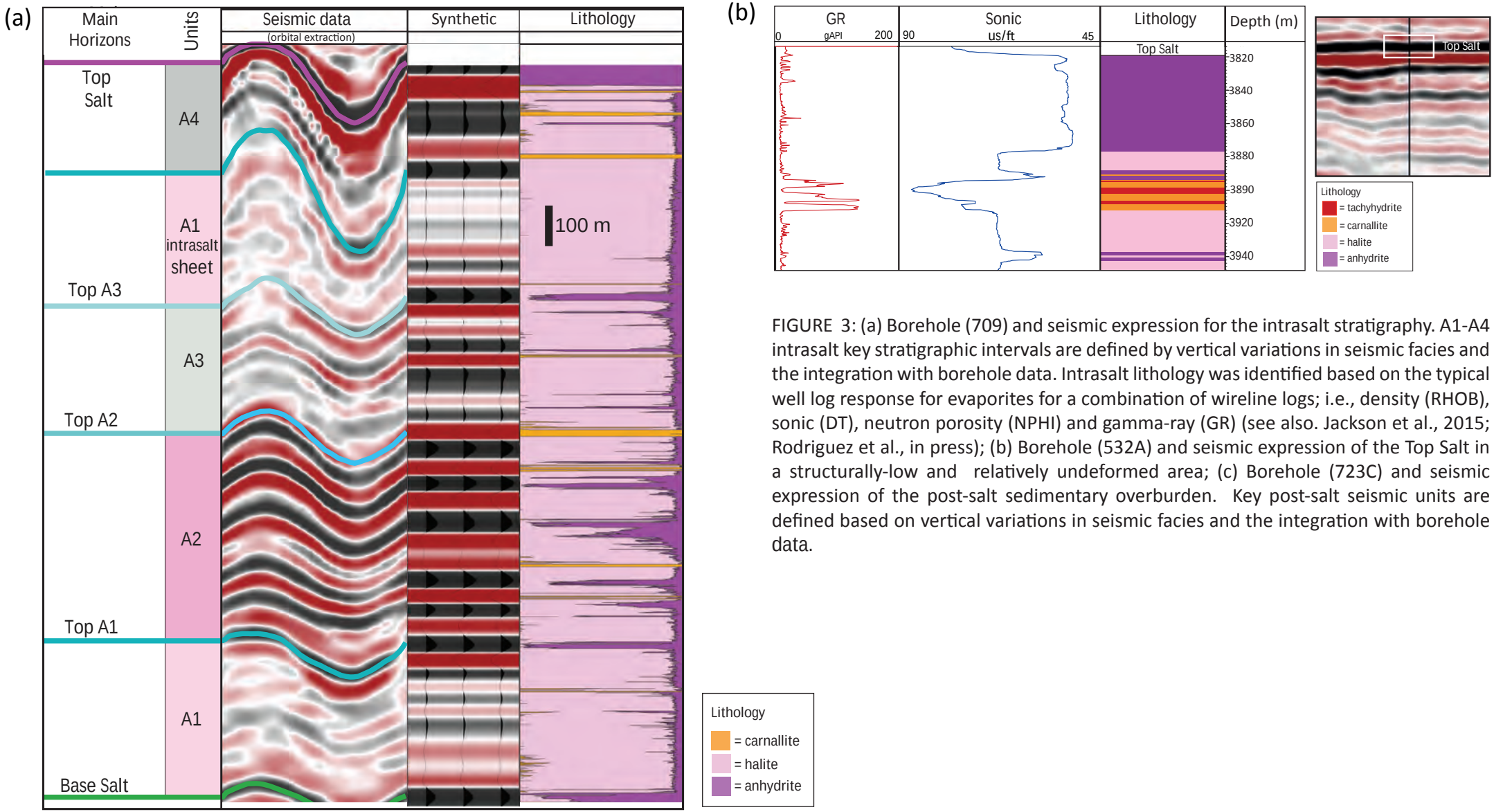

FIGURE 3: (a) Borehole (709) and seismic expression for the intrasalt stratigraphy. A1-A4 intrasalt key stratigraphic intervals are defined by vertical variations in seismic facies and the integration with borehole data. Intrasalt lithology was identified based on the typical well log response for evaporites for a combination of wireline logs; i.e., density (RHOB), sonic (DT), neutron porosity (NPHI) and gamma-ray (GR) (see also. Jackson et al., 2015; Rodriguez et al., in press); (b) Borehole (532A) and seismic expression of the Top Salt in a structurally-low and relatively undeformed area; (c) Borehole (723C) and seismic expression of the post-salt sedimentary overburden. Key post-salt seismic units are defined based on vertical variations in seismic facies and the integration with borehole data.

(c)

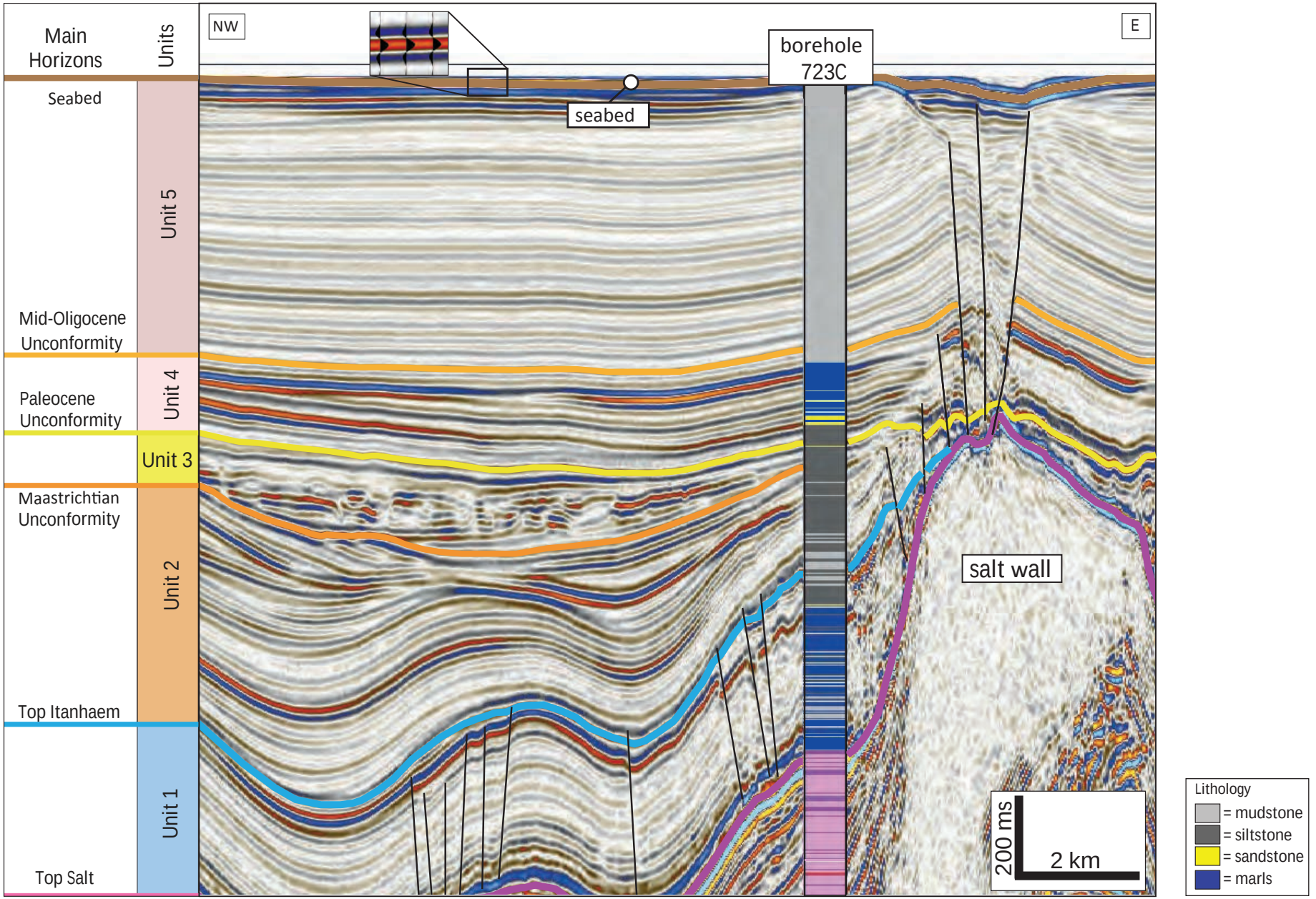
Main Horizons
Units
NW
E
borehole 723C
seabed
Seabed
Mid-Oligocene Unconformity
Paleocene Unconformity
Maastrichtian Unconformity
Top Itanhaem
Top Salt
Unit 5
Unit 4
Unit 3
Unit 2
Unit 1
salt wall
200 ms
2 km
Lithology
= mudstone
= siltstone
= sandstone
= marls

Table 2 : Overburden seismic expression and thickness variations above dissolved rugose crests.

Seismic facies		External shape relationship to salt crests	Amplitude, continuity reflection configuration	Ocurrence	Thickness variations	Interpretation
SF5	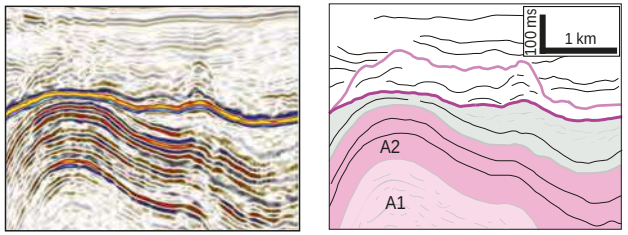	mound sub-parallel to intrasalt stratigraphy onlapped by overburden	low-to-moderate amplitudes discontinous suparallel to wavy to chaotic	Rugose crest-central Above truncated A3 reflections	mounds are thicker where more evaporites depletion is evident	Interpretation1: residual solution breccia or caprock composed by less-soluble and insoluble intrasalt and overburden lithology (e.g, anhydrite carbonates, fine-grained sediments) Interpretation 2: Carbonate reef deposited after dissolution of the underlying crest
SF6	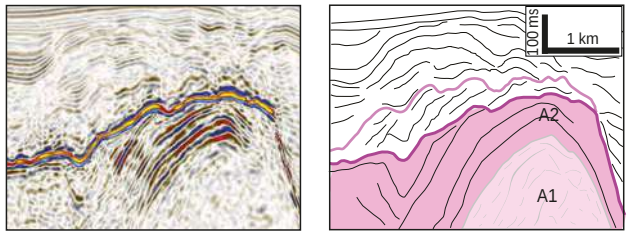	mound sub-parallel and follow the dips of underlying intrasalt stratigraphy	low-to-moderate amplitudes discontinous suparallel to wavy	Rugose crest - east Above truncated and tilted A2 reflections	mounds are thicker where more evaporites depletion is evident	
SF7	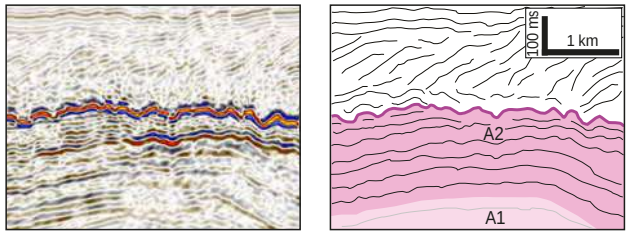	sheet downlapped by rotated overburden	low to moderate amplitudes chaotic subparallel to disrupted	Rugose crest - west Above truncated A2 reflections	overburden is thicker where more evaporites dissolution is evident	Dissolution at the crest led to rotation and collapse of the overbuden

Table 3: Overburden seismic expression and thickness variations above dissolved flat crests.

	Seismic facies	External shape relationship to salt crests	Amplitude, continuity reflection configuration	Ocurrence	Thickness variations	Interpretation
SF1	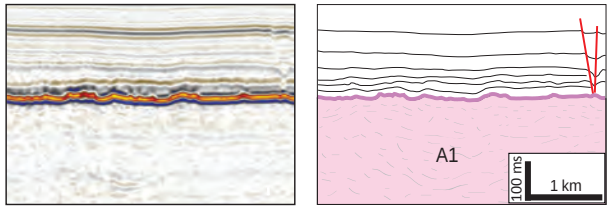	sheet drape conformable to top salt	low-to-moderate amplitudes continuous parallel to sub-parallel	Flat crest - east Above A1-allocthonous intrasalt sheet	minor thickness variations c.± 50ms local depocenters up to c.80ms above lows on top salt	fine-grained lithology deposited on flat crest before dissolution post-depositional dissolution not too obvious at seismic scale
SF2	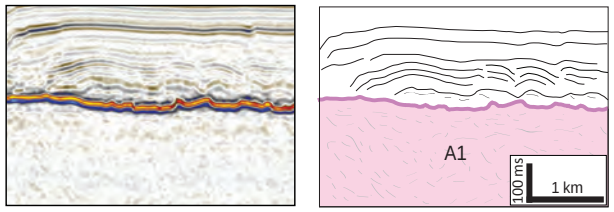	sheet to mound apparent downlap on top salt	low-to-moderate amplitudes semicontinuous to disrupted parallel to sub-parallel	Flat crest - central Above flat A1-allocthonous intrasalt sheet	minor thickness variations c.± 75 ms local depocenters up to c.125 ms above lows on top salt	fine-grained lithology deposited on salt crest before dissolution post-depositional dissolution led to local collapse and deformation within the overburden
SF3	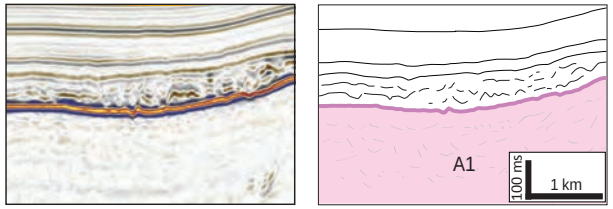	sheet to wedge conformable & apparent downlaps on top salt	low-to-moderate amplitudes discontinuous wavy to chaotic	Flat crest - central Above lows on A1-allocthonous intrasalt sheet	minor thickness variations c.± 75 ms local depocenters up to c.125 ms above lows on top salt	fine-grained lithology deposited on salt crest before dissolution post-depositional dissolution led to local collapse and deformation within the overburden
SF4	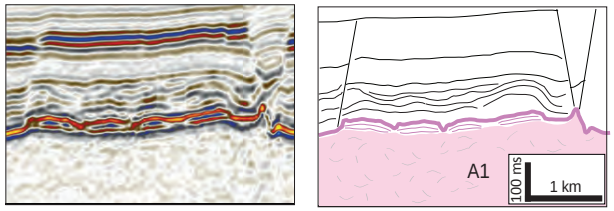	sheet to mound conformable & apparent downlaps on top salt	moderate to high amplitudes semicontinuos subparallel to wavy	Flat crest - west Above discrete mounds on top salt	minor thickness variations c.± 100 ms local depocenters up to c.150 ms above lows on top salt	fine-grained lithology deposited on salt crest during dissolution syn-depositional dissolution led to local collapse and deformation within the overburden

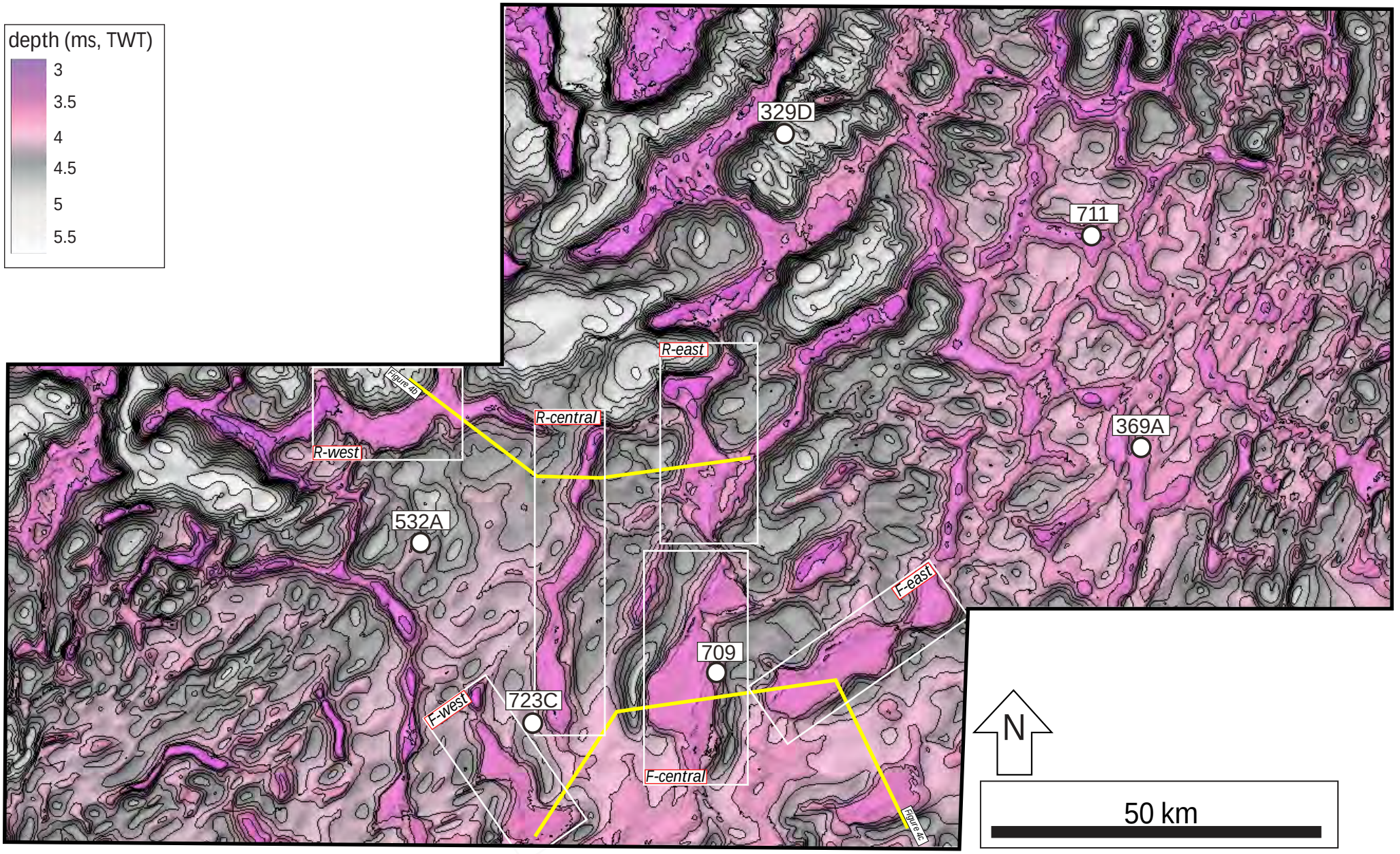

FIGURE 4: (a) Top salt structural map with locations of salt walls of interest

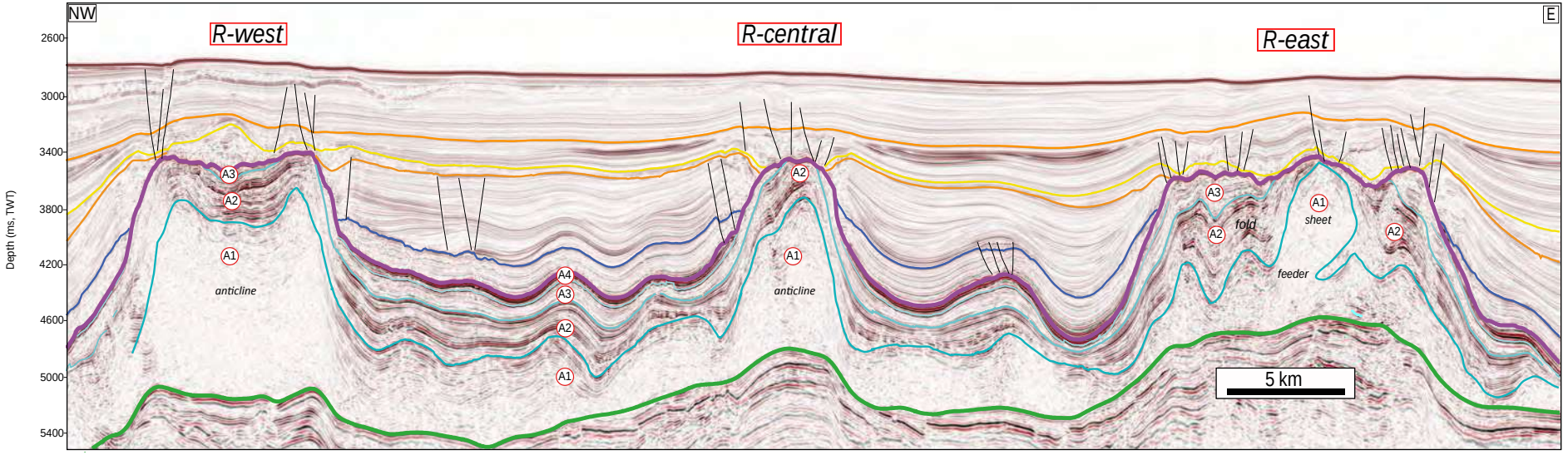

Figure 4 b: Seismic section across salt diapirs with rounded and rugose crests

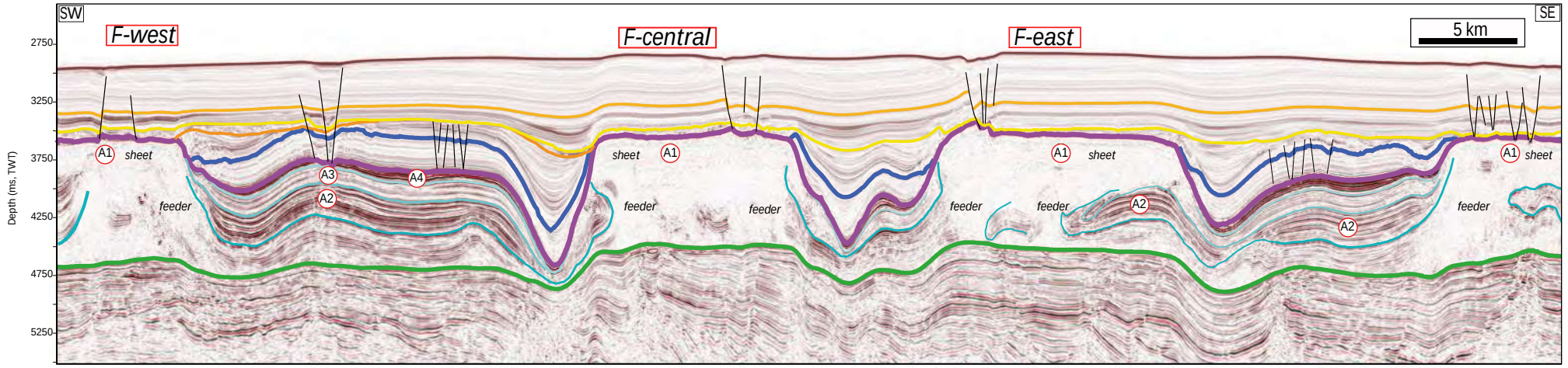

Figure 4 c: Seismic section across salt diapirs with flat crests

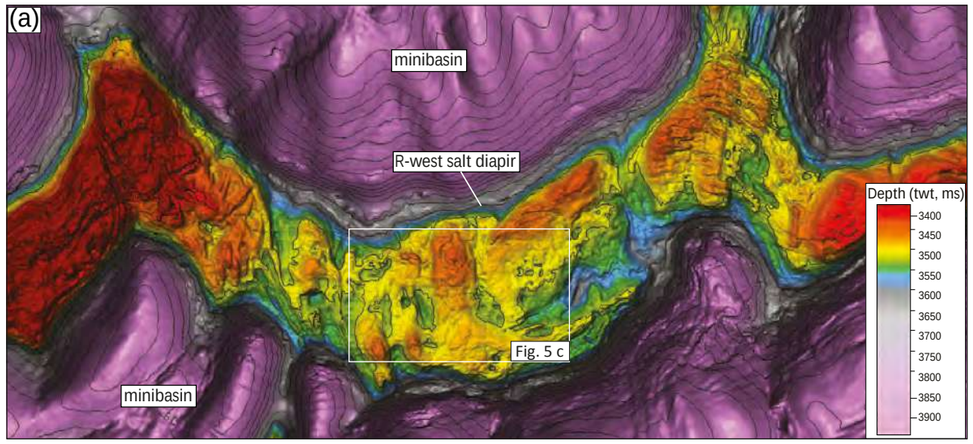

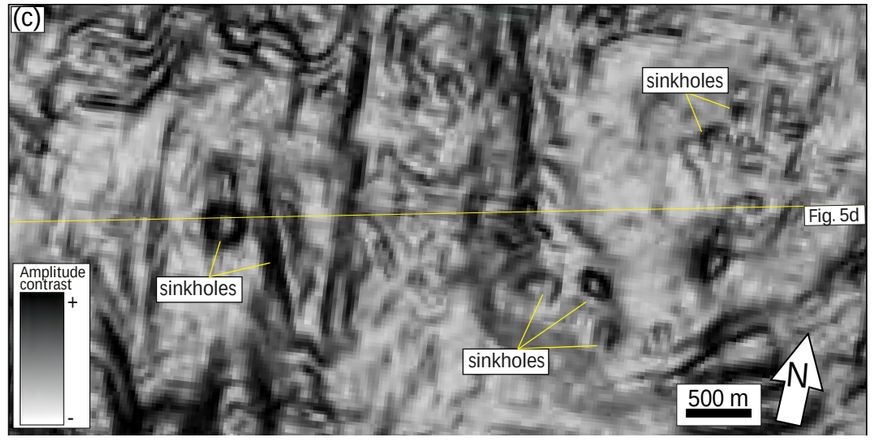

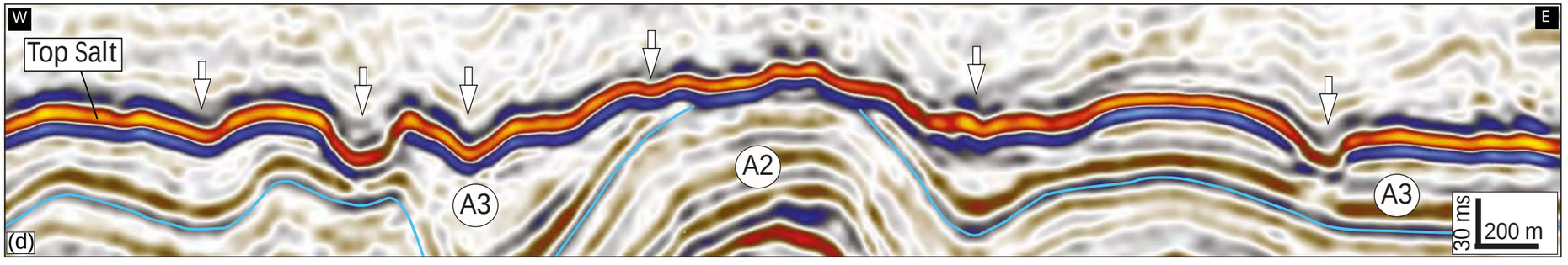

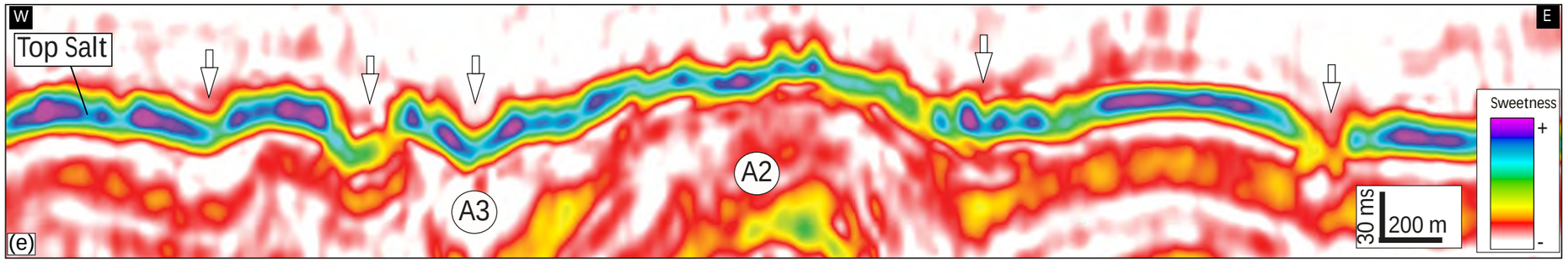

FIGURE 5: Seismic expression of salt dissolution-related sinkholes: (a) R-west top salt structural map; (b) Salt karst along Top Salt and intrasalt stratigraphy subcropping the R-west salt diapir; (c) Amplitude contrast attribute map for R-west Top Salt highlighting the sinkholes along Top Salt, see Figure 5a for location; (d) Seismic section along the crest of R-east illustrating the geometry of sinkholes (indicated by white arrows) and their relationship to halite-rich A3 intrasalt unit. Location is shown on Figure 5c; (e) Sweetness attribute of the seismic section on (d)

FIGURE 6: Seismic expression of salt dissolution-related sinkholes: (a) R-east top salt structural map; (b) Salt karst along Top Salt and Intrasalt stratigraphy subcropping R-east salt diapir; (c) Amplitude contrast attribute map for R-east Top Salt highlighting the sinkholes along Top Salt, see Figure 6a for location; (d) Seismic section along the crest of R-east illustrating the geometry of sinkholes (indicated by white arrows) and their relationship to dipping-A2 intrasalt stratigraphy. Location is shown on Figure 6c; (e) Chaos attribute of the seismic section on Figure 6d highlighting the sinkholes along the Top Salt.

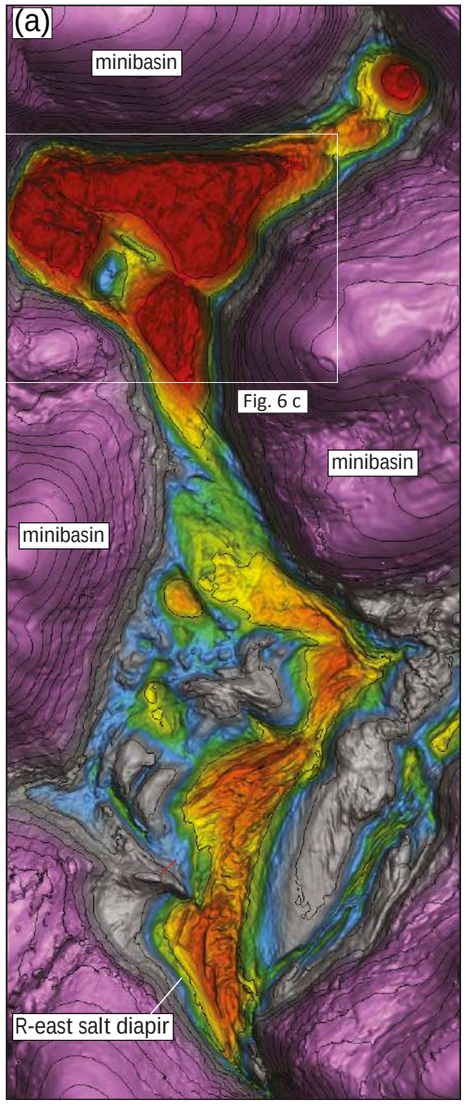

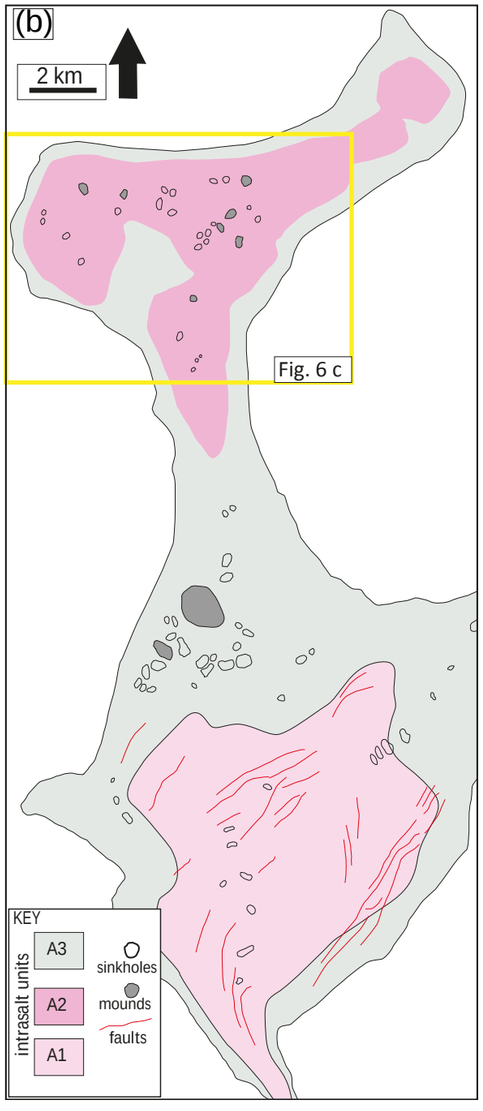

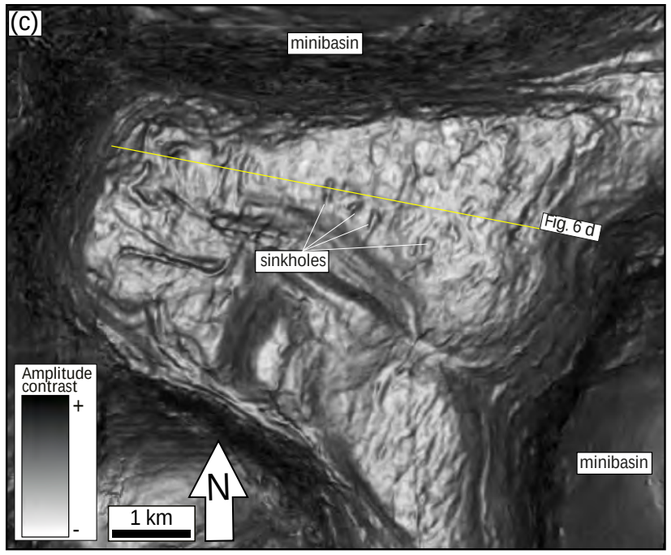

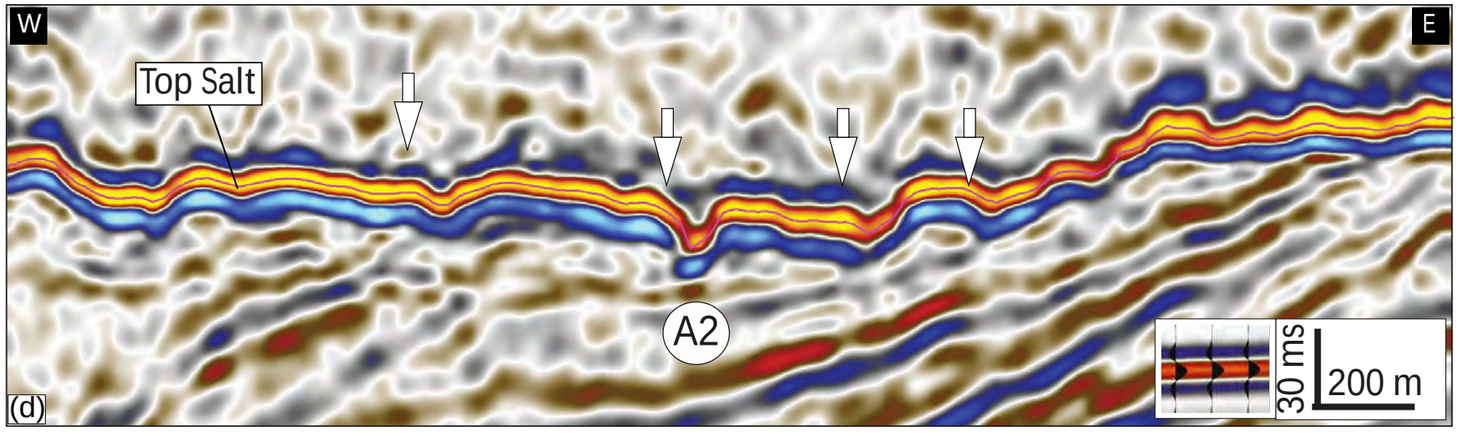

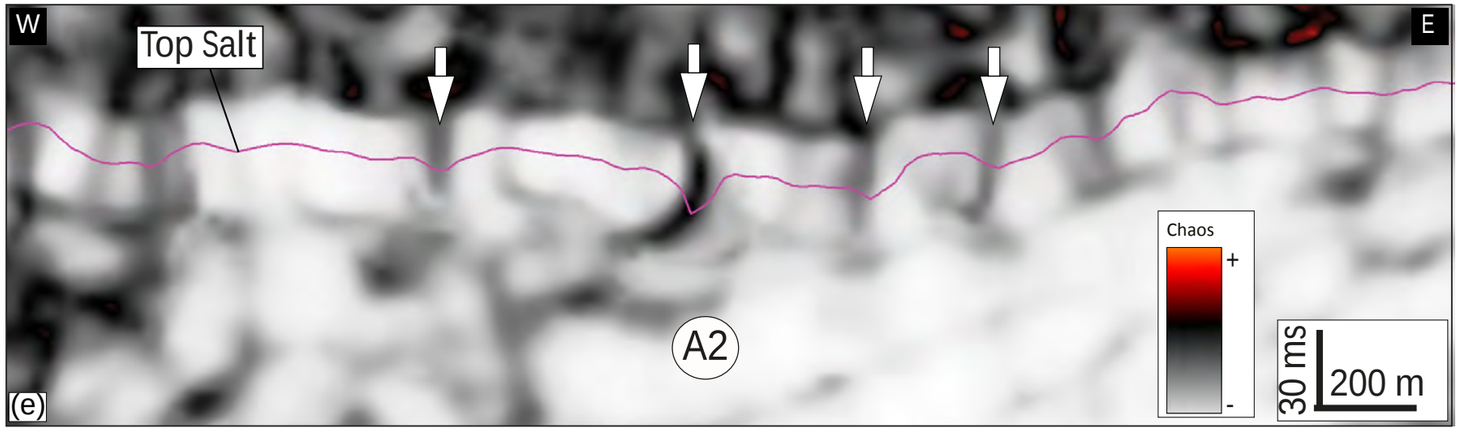

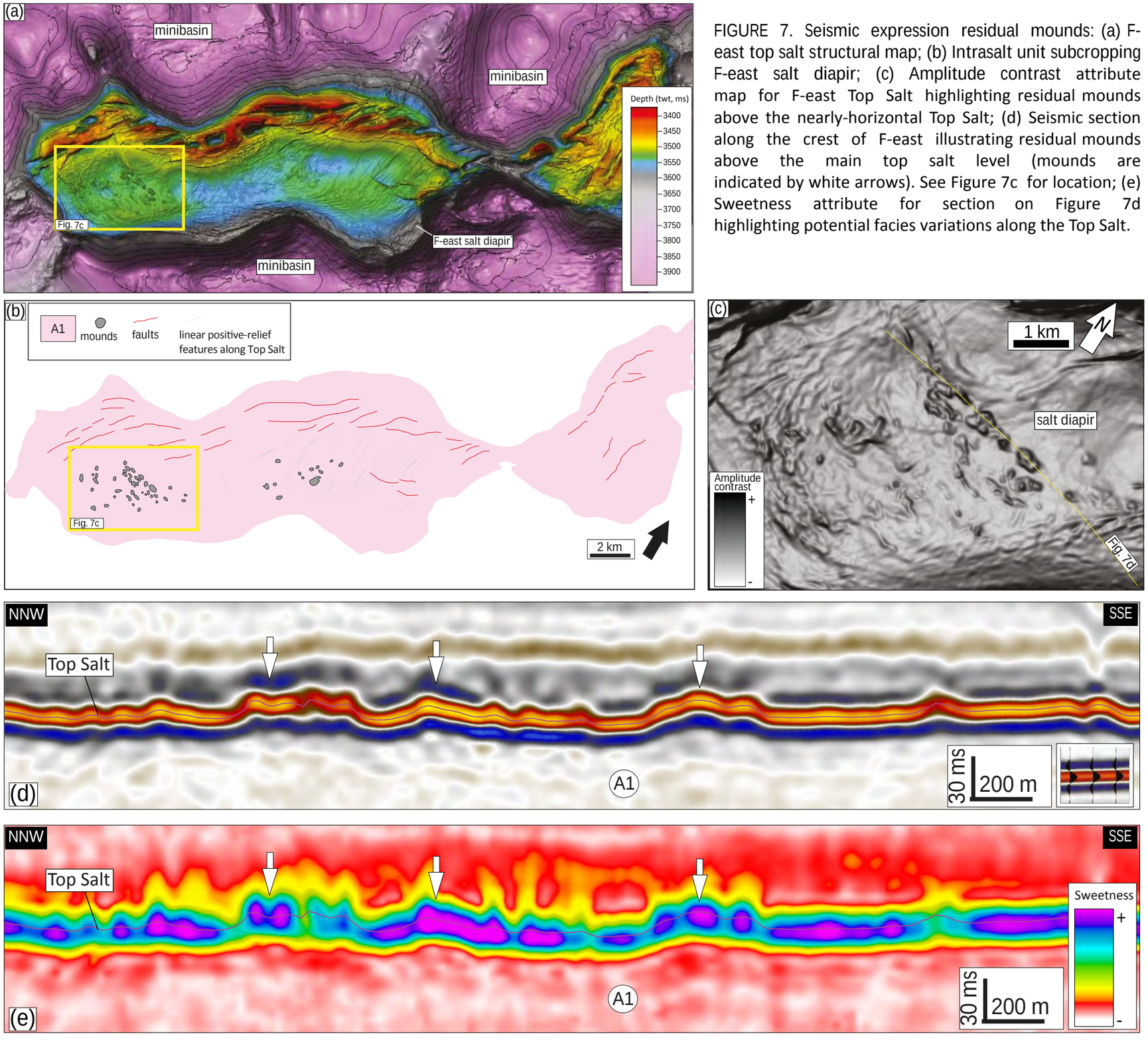

FIGURE 7. Seismic expression residual mounds: (a) F-east top salt structural map; (b) Intrasalt unit subcropping F-east salt diapir; (c) Amplitude contrast attribute map for F-east Top Salt highlighting residual mounds above the nearly-horizontal Top Salt; (d) Seismic section along the crest of F-east illustrating residual mounds above the main top salt level (mounds are indicated by white arrows). See Figure 7c for location; (e) Sweetness attribute for section on Figure 7d highlighting potential facies variations along the Top Salt.

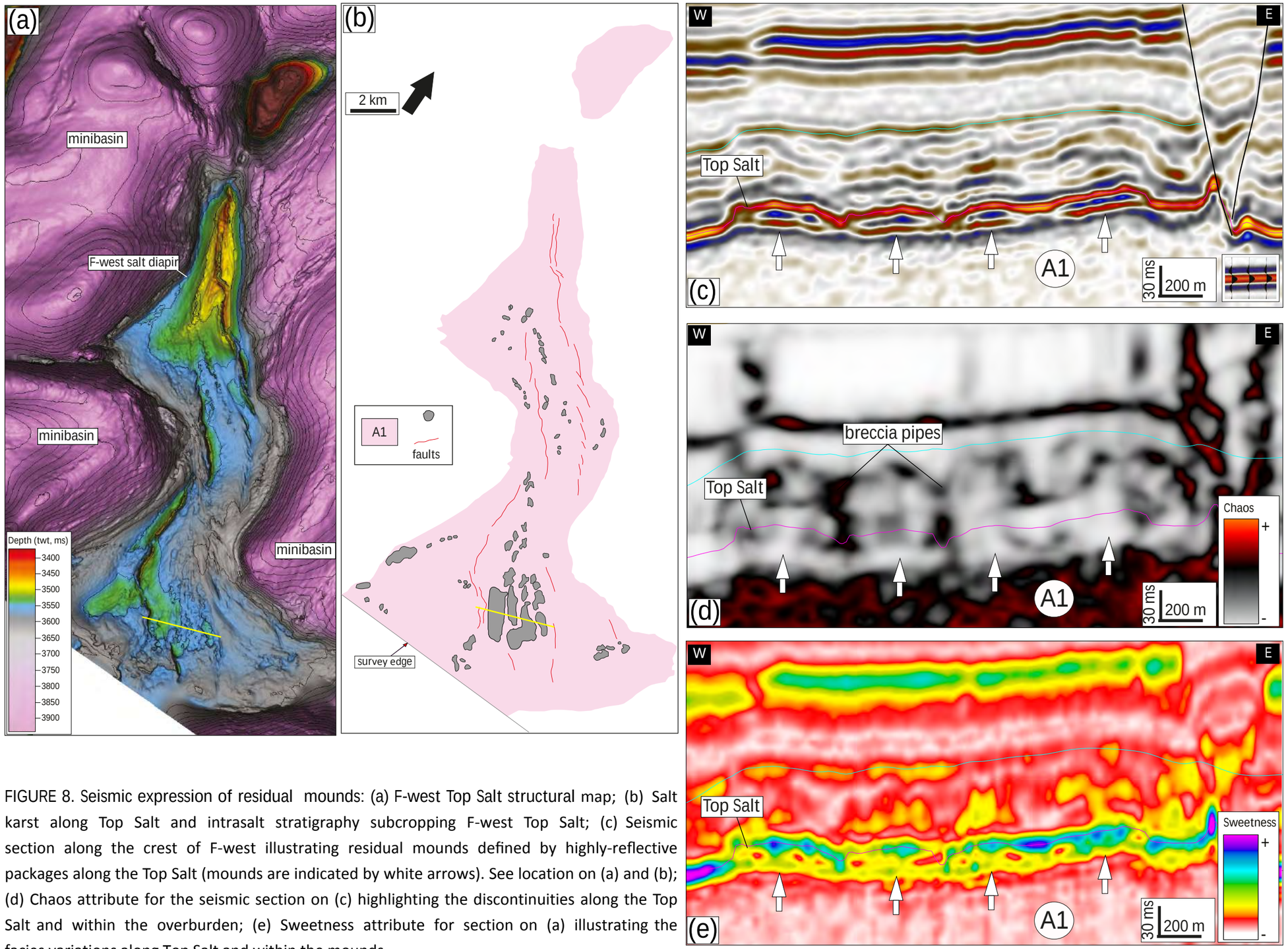

FIGURE 8. Seismic expression of residual mounds: (a) F-west Top Salt structural map; (b) Salt karst along Top Salt and intrasalt stratigraphy subcropping F-west Top Salt; (c) Seismic section along the crest of F-west illustrating residual mounds defined by highly-reflective packages along the Top Salt (mounds are indicated by white arrows). See location on (a) and (b); (d) Chaos attribute for the seismic section on (c) highlighting the discontinuities along the Top Salt and within the overburden; (e) Sweetness attribute for section on (a) illustrating the facies variations along Top Salt and within the mounds

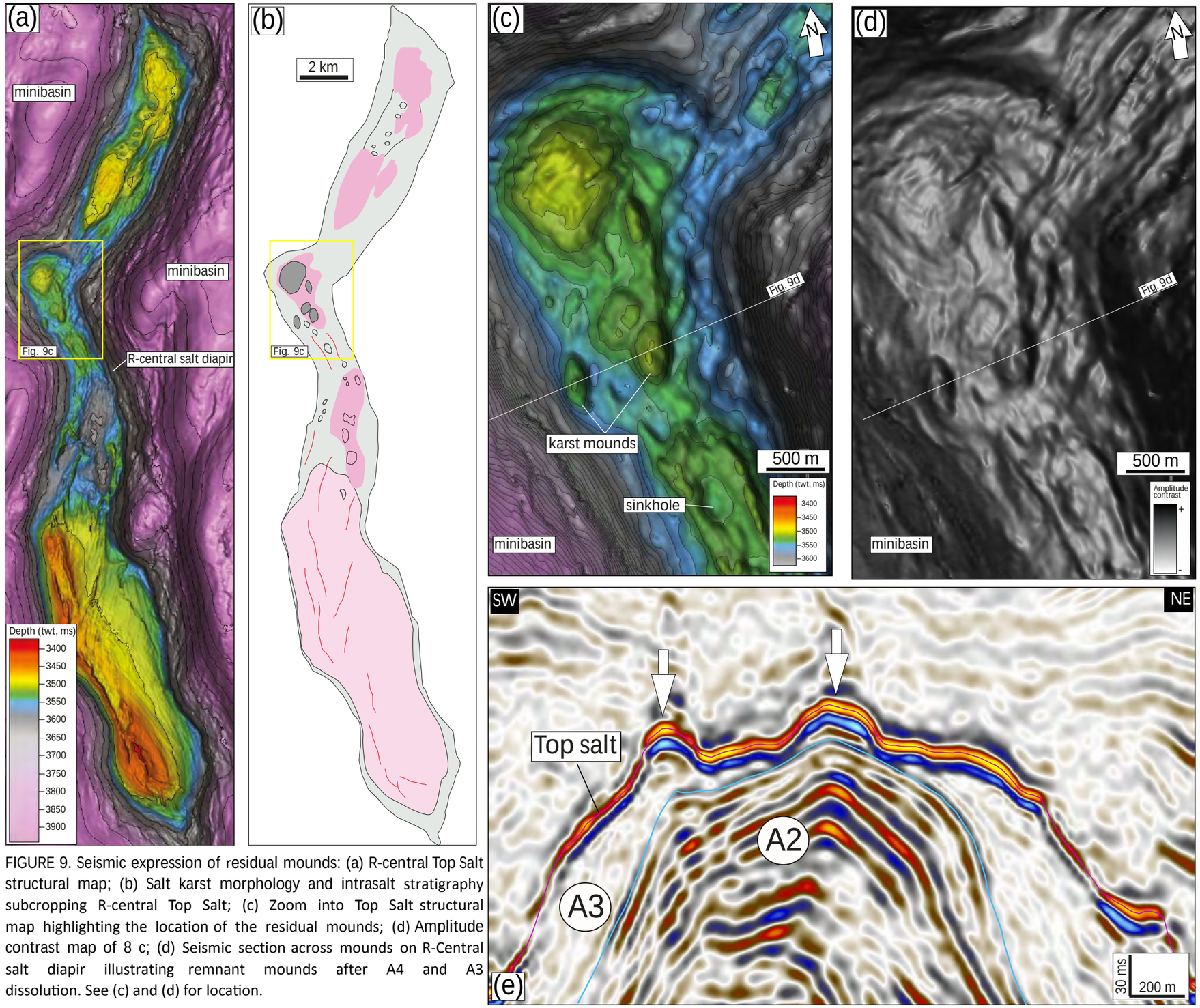

FIGURE 9. Seismic expression of residual mounds: (a) R-central Top Salt structural map; (b) Salt karst morphology and intrasalt stratigraphy subcropping R-central Top Salt; (c) Zoom into Top Salt structural map highlighting the location of the residual mounds; (d) Amplitude contrast map of 8 c; (d) Seismic section across mounds on R-Central salt diapir illustrating remnant mounds after A4 and A3 dissolution. See (c) and (d) for location.

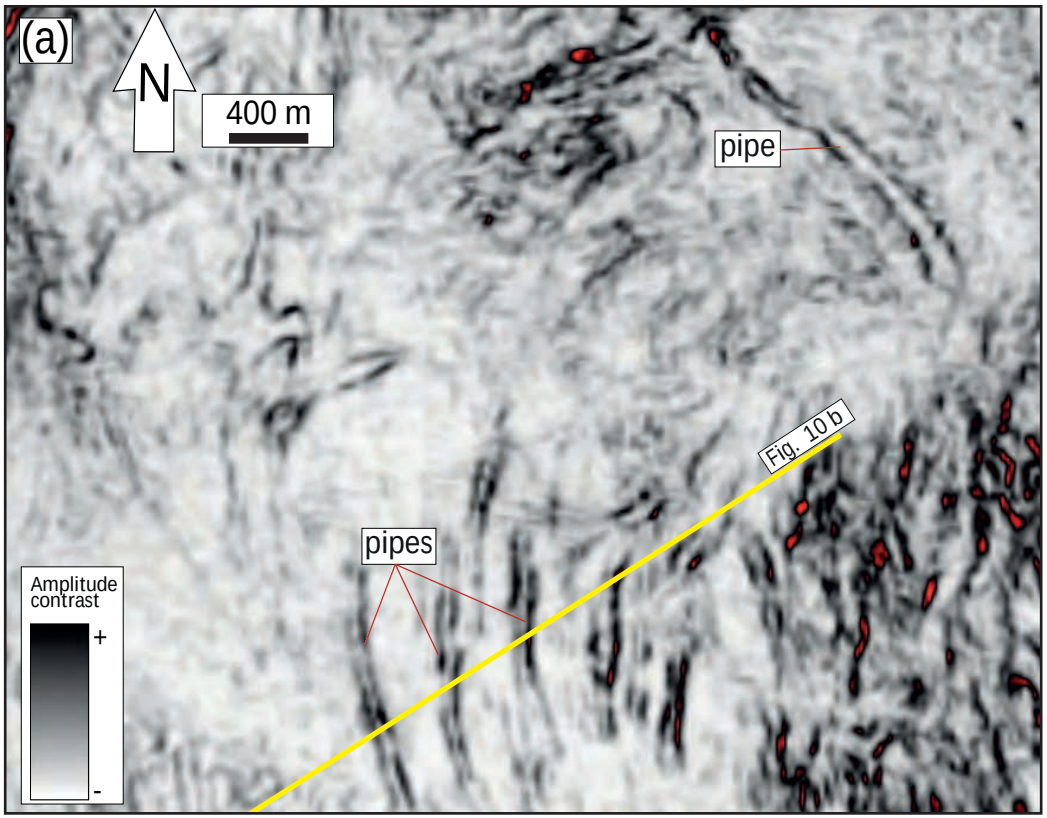

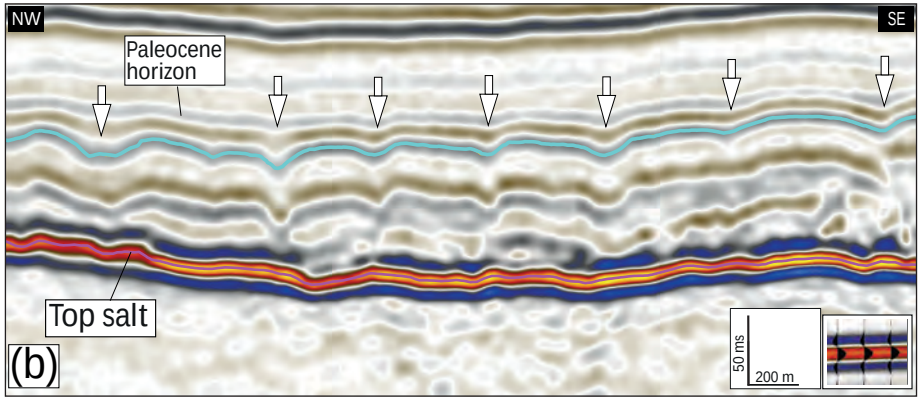

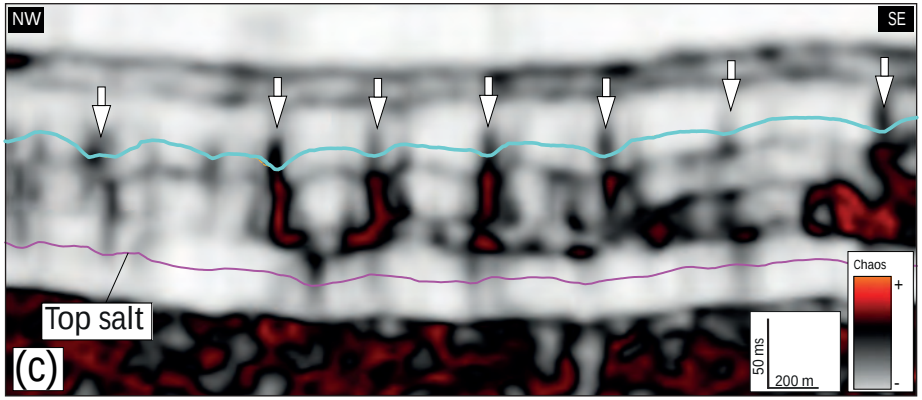

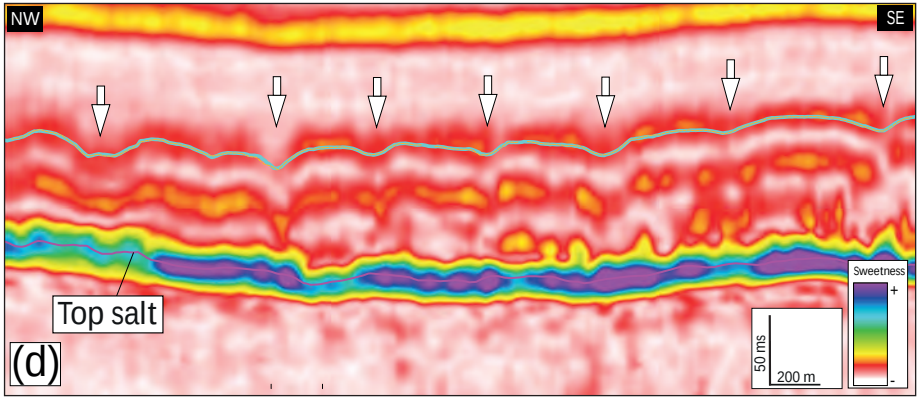

FIGURE 10: Seismic expression of breccia pipes or chimneys within the overburden: (a) Amplitude contrast seismic attribute time slice highlighting the edges of the breccia pipes. See location on Figure 11a; (b) Seismic section accross the crest of F-central and overburden strata. Breccia Pipes are indicated with white arrows; (c) Chaos seismic attribute for the section on Figure 10b highlighting the breccias cross-cutting the overburden strata; (d) Sweetness seismic attribute for the section on Figure 10b. Some of the breccia pipes correlate with facies variations along the Top Salt.

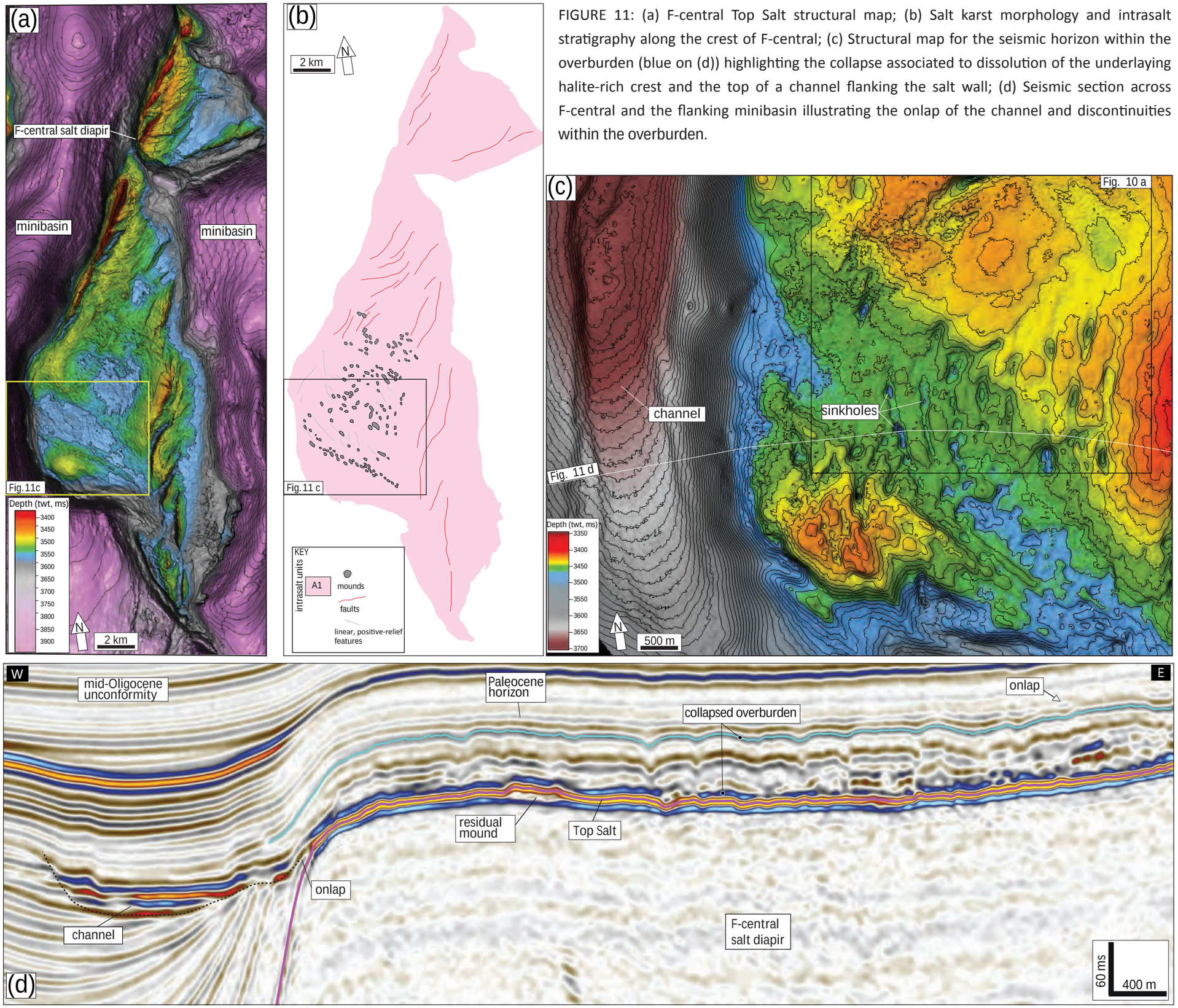

FIGURE 11: (a) F-central Top Salt structural map; (b) Salt karst morphology and intrasalt stratigraphy along the crest of F-central; (c) Structural map for the seismic horizon within the overburden (blue on (d)) highlighting the collapse associated to dissolution of the underlaying halite-rich crest and the top of a channel flanking the salt wall; (d) Seismic section across F-central and the flanking minibasin illustrating the onlap of the channel and discontinuities within the overburden.

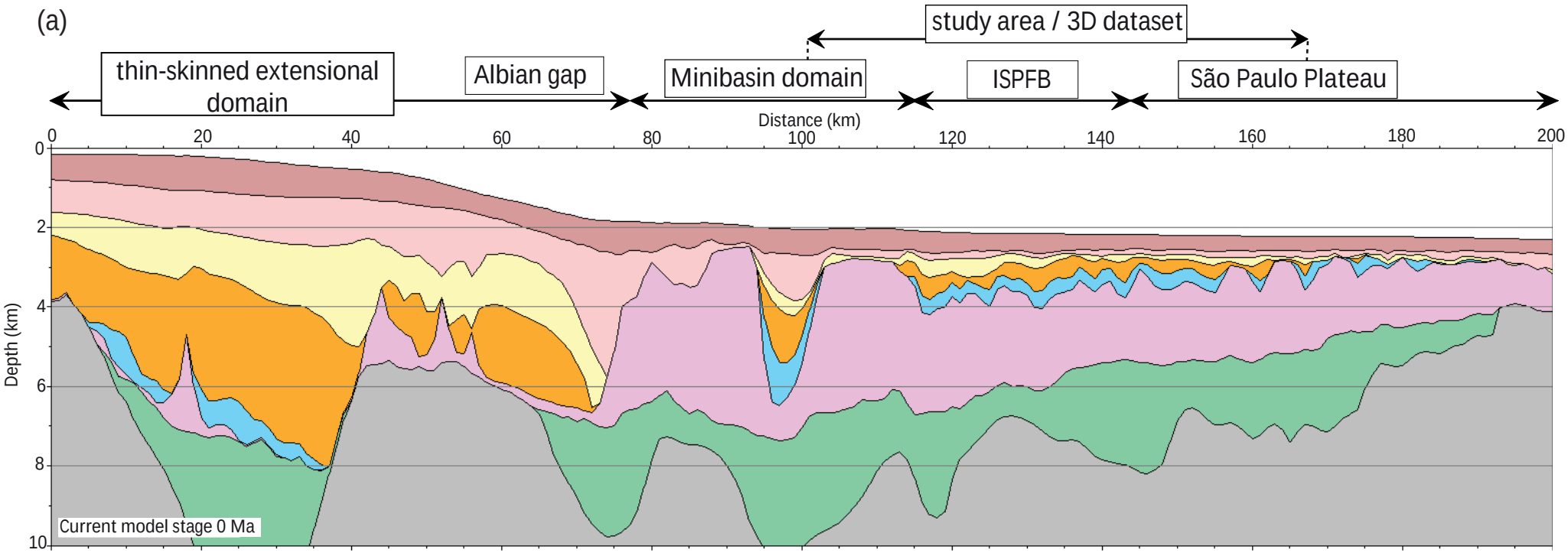

FIGURE 12: (a) Input model used for basin restoration based on the interpretation of 2D depth seismic profile (Figure 2b). See Key on Figure 2a; (b) Minimum Beta Stretching Factor along the 2D seismic profile (after Scotchman et al., 2006); (c) Maximum Beta Stretching Factor along the 2D seismic profile (after Scotchman et al., 2006); (d) Basin restoration to the mid-Oligocene (28 Ma) based on the minimum Beta Stretching Factor profile; (e) Basin restoration to the mid-Oligocene (28 Ma) based on the maximum Beta Stretching Factor profile; (f) Basin restoration to the Paleocene (60 Ma) based on the minimum Beta Stretching Factor profile; (f) Basin restoration to the Paleocene (60 Ma) based on the maximum Beta Stretching Factor profile

(b)

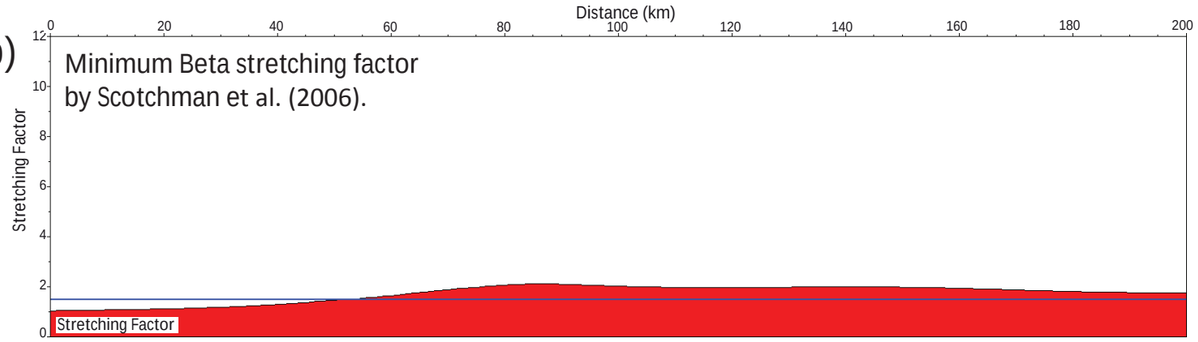
Minimum Beta stretching factor
by Scotchman et al. (2006).
Distance (km)
Stretching Factor
Stretching Factor

(c)

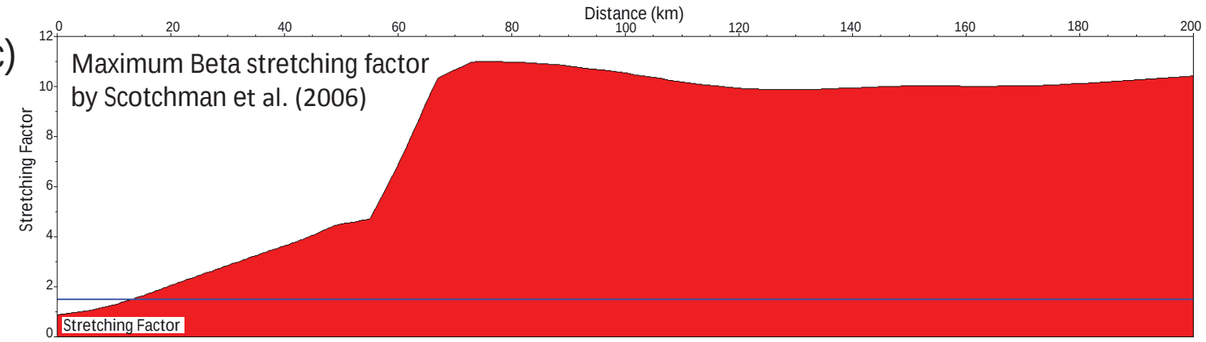
Maximum Beta stretching factor
by Scotchman et al. (2006)
Distance (km)
Stretching Factor
Stretching Factor

(d)

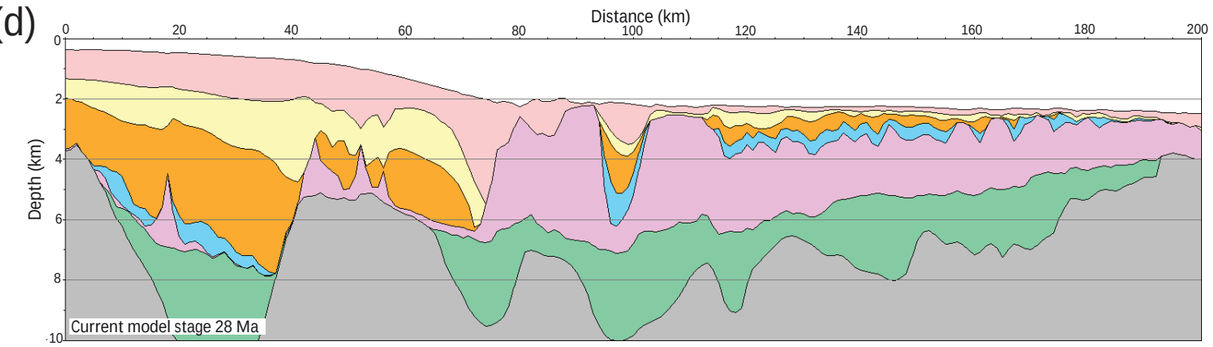
Distance (km)
Depth (km)
Current model stage 28 Ma

(e)

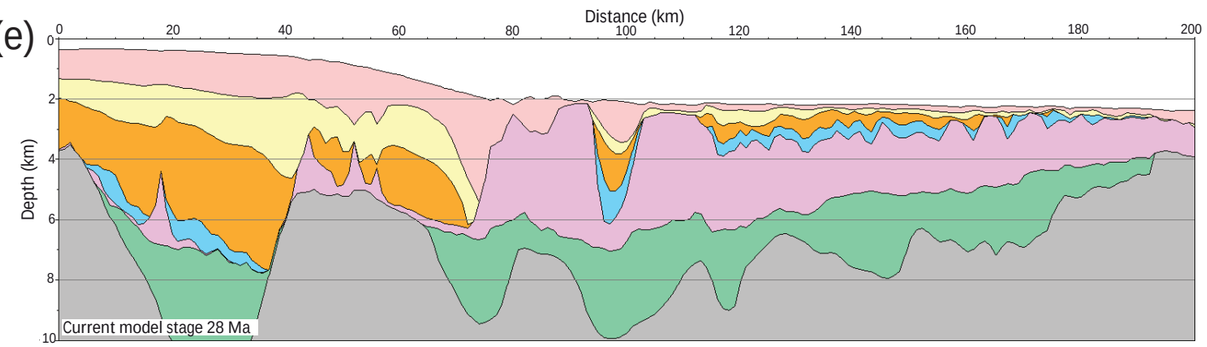
Distance (km)
Depth (km)
Current model stage 28 Ma

(f)

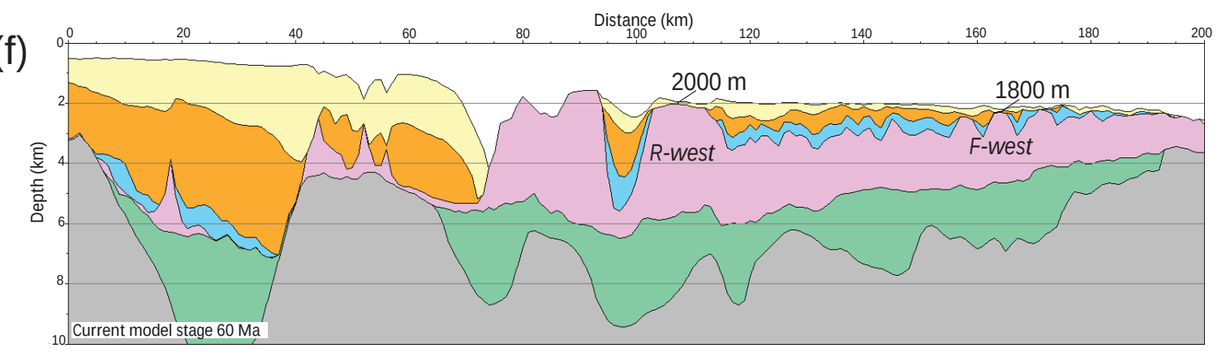
Distance (km)
2000 m
1800 m
R-west
F-west
Depth (km)
Current model stage 60 Ma

(g)

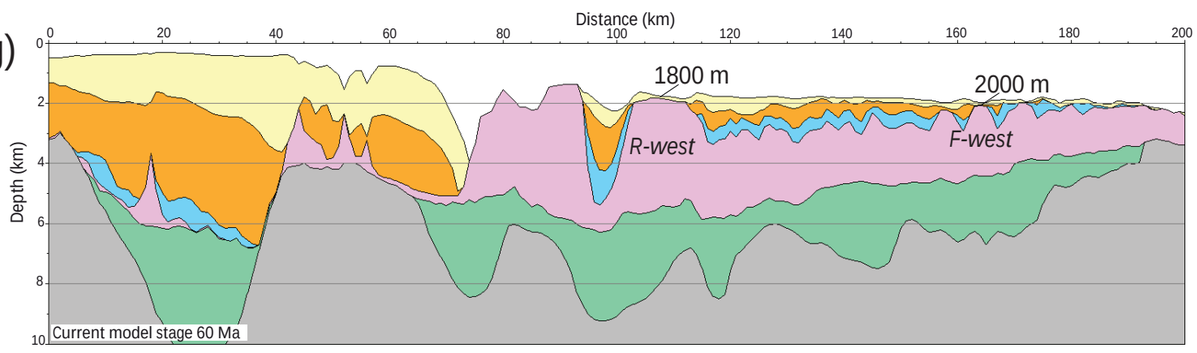
Distance (km)
1800 m
2000 m
R-west
F-west
Depth (km)
Current model stage 60 Ma

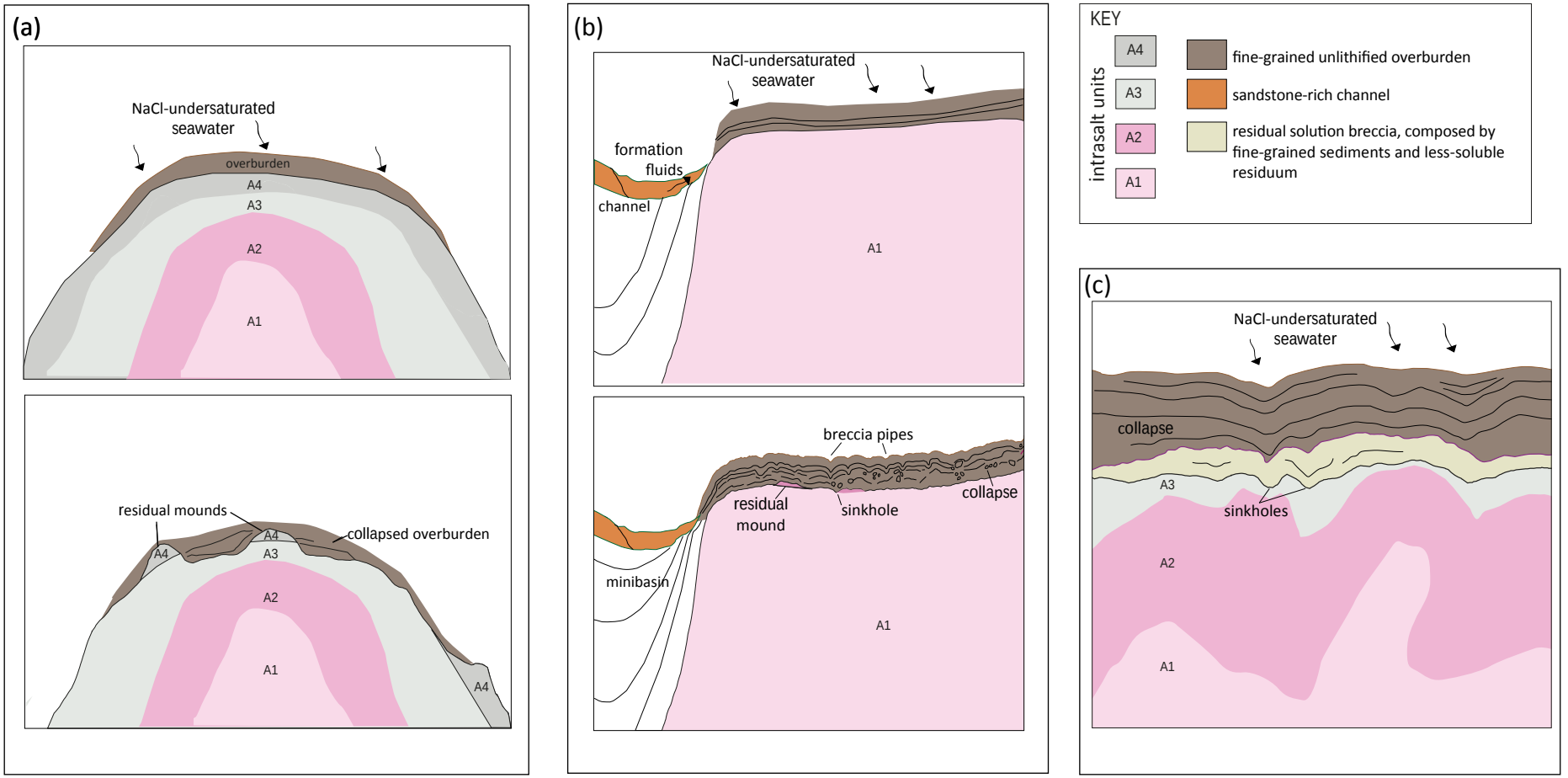

FIGURE 13: Mechanisms and styles of submarine salt dissolution: (a) Superjacent dissolution by NaCl-undersaturated seawater penetrating the very fine-grained, unlithified overburden during exposure at the seafloor; (b) Dissolution due to fluids migrating from carrier beds directly in contact with the salt; (c) Residual Solution breccia formed by the preferential depletion of the evaporite-dominated crests and collapse of the overburden.